

NIST Special Publication 1018-5

# Fire Dynamics Simulator (Version 5) Technical Reference Guide

Volume 2: Verification

Randall McDermott

Kevin McGrattan

Simo Hostikka

Jason Floyd



NIST Special Publication 1018-5

# Fire Dynamics Simulator (Version 5) Technical Reference Guide

## Volume 2: Verification

Randall McDermott  
Kevin McGrattan  
*Fire Research Division  
Building and Fire Research Laboratory*

Simo Hostikka  
*VTT Technical Research Centre of Finland  
Espoo, Finland*

Jason Floyd  
*Hughes Associates, Inc.  
Baltimore, Maryland*

September 1, 2009  
FDS Version 5.4  
*SVNRepository Revision : 4651*



U.S. Department of Commerce  
*Gary Locke, Secretary*

National Institute of Standards and Technology  
*Patrick Gallagher, Acting Director*



# Preface

This is Volume 2 of the FDS Technical Reference Guide. Volume 1 describes the mathematical model and numerical method. Volume 3 documents past and present experimental validation work. Instructions for using FDS are contained in a separate User's Guide [1].

The three volumes of the FDS Technical Reference Guide are based in part on the “Standard Guide for Evaluating the Predictive Capability of Deterministic Fire Models,” ASTM E 1355 [2]. ASTM E 1355 defines *model evaluation* as “the process of quantifying the accuracy of chosen results from a model when applied for a specific use.” The model evaluation process consists of two main components: verification and validation. *Verification* is a process to check the correctness of the solution of the governing equations. Verification does not imply that the governing equations are appropriate; only that the equations are being solved correctly. *Validation* is a process to determine the appropriateness of the governing equations as a mathematical model of the physical phenomena of interest. Typically, validation involves comparing model results with experimental measurement. Differences that cannot be explained in terms of numerical errors in the model or uncertainty in the measurements are attributed to the assumptions and simplifications of the physical model.

Evaluation is critical to establishing both the acceptable uses and limitations of a model. Throughout its development, FDS has undergone various forms of evaluation, both at NIST and beyond. This volume provides a survey of verification work conducted to date to evaluate FDS.



# About the Authors

**Randall McDermott** joined the research staff of the Building and Fire Research Lab in 2008. He received a B.S. degree from the University of Tulsa in Chemical Engineering in 1994 and a doctorate at the University of Utah in 2005. His research interests include subgrid-scale models and numerical methods for large-eddy simulation, adaptive mesh refinement, and Lagrangian particle methods.

**Kevin McGrattan** is a mathematician in the Building and Fire Research Laboratory (BFRL) of NIST. He received a bachelors of science degree from the School of Engineering and Applied Science of Columbia University in 1987 and a doctorate at the Courant Institute of New York University in 1991. He joined the NIST staff in 1992 and has since worked on the development of fire models, most notably the Fire Dynamics Simulator.

**Simo Hostikka** is a Senior Research Scientist at VTT Technical Research Centre of Finland. He received a master of science (technology) degree in 1997 and a doctorate in 2008 from the Department of Engineering Physics and Mathematics of the Helsinki University of Technology. He is the principal developer of the radiation and solid phase sub-models within FDS.

**Jason Floyd** is a Senior Engineer at Hughes Associates, Inc., in Baltimore, Maryland. He received a bachelors of science and Ph.D. in the Nuclear Engineering Program of the University of Maryland. After graduating, he won a National Research Council Post-Doctoral Fellowship at the Building and Fire Research Laboratory of NIST, where he developed the combustion algorithm within FDS. He is currently funded by NIST under grant 70NANB8H8161 from the Fire Research Grants Program (15 USC 278f). He is the principal developer of the multi-parameter mixture fraction combustion model and control logic within FDS.





# Acknowledgments

Partial support for the preparation of the FDS Technical Reference Guides has been provided by the Office of Nuclear Regulatory Research of the US Nuclear Regulatory Commission (US NRC). Special thanks to Mark Salley and Jason Dreisbach for their efforts.

Thanks to Chris Lautenburger and Carlos Fernandez-Pello for their assistance with the “two-reaction” test case.



# Contents

<b>Preface</b>	<b>i</b>
<b>About the Authors</b>	<b>iii</b>
<b>Acknowledgments</b>	<b>v</b>
<b>1 What is Verification?</b>	<b>1</b>
<b>2 Survey of Past Verification Work</b>	<b>3</b>
2.1 Analytical Tests . . . . .	3
2.2 Numerical Tests . . . . .	4
2.3 Sensitivity Analysis . . . . .	5
2.3.1 Grid Sensitivity . . . . .	5
2.3.2 Sensitivity of Large Eddy Simulation Parameters . . . . .	7
2.3.3 Sensitivity of Radiation Parameters . . . . .	7
2.3.4 Sensitivity of Thermophysical Properties of Solid Fuels . . . . .	8
2.4 Code Checking . . . . .	9
<b>3 The Basic Flow Solver</b>	<b>11</b>
3.1 2D Analytical Solution to Navier-Stokes . . . . .	11
3.2 Decaying Isotropic Turbulence . . . . .	15
3.3 The Dynamic Smagorinsky Model . . . . .	18
3.4 FDS Wall Flows Part I: Straight Channels . . . . .	20
3.4.1 Formulation . . . . .	20
3.4.2 The Werner and Wengle Wall Model . . . . .	20
3.4.3 Results . . . . .	22
3.4.4 Conclusions . . . . .	24
<b>4 Thermal Radiation</b>	<b>27</b>
4.1 Radiation inside a box ( <b>radiation_in_a_box</b> ) . . . . .	28
4.2 Radiation from a plane layer ( <b>radiation_plane_layer</b> ) . . . . .	29
4.3 Wall Internal Radiation ( <b>wall_internal_radiation</b> ) . . . . .	30
<b>5 Heat Conduction</b>	<b>31</b>
5.1 Simple Heat Conduction Through a Solid Slab ( <b>heat_conduction</b> ) . . . . .	32
5.2 Temperature-Dependent Thermal Properties ( <b>heat_conduction_kc</b> ) . . . . .	33

<b>6</b>	<b>Pyrolysis</b>	<b>35</b>
6.1	A Simple Two-Step Pyrolysis Example ( <b>two_step_solid_reaction</b> ) . . . . .	36
6.2	Development of surface emissivity ( <b>emissivity</b> ) . . . . .	37
6.3	Enthalpy of solid materials ( <b>enthalpy</b> ) . . . . .	38
6.4	Using TGA Data ( <b>birch_tga</b> ) . . . . .	39
<b>7</b>	<b>Droplets</b>	<b>41</b>
7.1	Water Droplet Evaporation ( <b>water_evaporation</b> ) . . . . .	41
	<b>Bibliography</b>	<b>43</b>

# Chapter 1

## What is Verification?

The terms *verification* and *validation* are often used interchangeably to mean the process of checking the accuracy of a numerical model. For many, this entails comparing model predictions with experimental measurements. However, there is now a fairly broad-based consensus that comparing model and experiment is largely what is considered *validation*. So what is *verification*? ASTM E 1355 [2], “Standard Guide for Evaluating the Predictive Capability of Deterministic Fire Models,” defines verification as

The process of determining that the implementation of a calculation method accurately represents the developer’s conceptual description of the calculation method and the solution to the calculation method.

and it defines validation as

The process of determining the degree to which a calculation method is an accurate representation of the real world from the perspective of the intended uses of the calculation method.

Simply put, verification is a check of the math; validation is a check of the physics. If the model predictions closely match the results of experiments, using whatever metric is appropriate, it is assumed by most that the model suitably describes, via its mathematical equations, what is happening. It is also assumed that the solution of these equations must be correct. So why do we need to perform model verification? Why not just skip to validation and be done with it? The reason is that rarely do model and measurement agree so well in all applications that anyone would just accept its results unquestionably. Because there is inevitably differences between model and experiment, we need to know if these differences are due to limitations or errors in the numerical solution, or the physical sub-models, or both.

Whereas model validation consists mainly of comparing predictions with measurements, as documented for FDS in Volume 3 of the Technical Reference Guide, model verification consists of a much broader range of activities, from checking the computer program itself to comparing calculations to analytical (exact) solutions to considering the sensitivity of the dozens of numerical parameters. The next chapter discusses these various activities, and the rest of the Guide is devoted mainly to comparisons of various sub-model calculations with analytical solutions.



## Chapter 2

# Survey of Past Verification Work

This chapter documents work of the past few decades at NIST, VTT and elsewhere to verify the algorithms within FDS.

### 2.1 Analytical Tests

Most complex combustion processes, including fire, are turbulent and time-dependent. There are no closed-form mathematical solutions for the fully-turbulent, time-dependent Navier-Stokes equations. CFD provides an approximate solution for the non-linear partial differential equations by replacing them with discretized algebraic equations that can be solved using a powerful computer. While there is no general analytical solution for fully-turbulent flows, certain sub-models address phenomenon that do have analytical solutions, for example, one-dimensional heat conduction through a solid. These analytical solutions can be used to test sub-models within a complex code such as FDS. The developers of FDS routinely use such practices to verify the correctness of the coding of the model [3, 4]. Such verification efforts are relatively simple and routine and the results may not always be published nor included in the documentation. Examples of routine analytical testing include:

- The radiation solver has been verified with scenarios where simple objects, like cubes or flat plates, are positioned in simple, sealed compartments. All convective motion is turned off, the object is given a fixed surface temperature and emissivity of one (making it a black body radiator). The heat flux to the cold surrounding walls is recorded and compared to analytical solutions. These studies help determine the appropriate number of solid angles to be set as the default.
- Solid objects are heated with a fixed heat flux, and the interior and surface temperatures as a function of time are compared to analytical solutions of the one-dimensional heat transfer equation. These studies help determine the number of nodes to use in the solid phase heat transfer model. Similar studies are performed to check the pyrolysis models for thermoplastic and charring solids.
- Early in its development, the hydrodynamic solver that evolved to form the core of FDS was checked against analytical solutions of simplified fluid flow phenomena. These studies were conducted at the National Bureau of Standards (NBS)<sup>1</sup> by Rehm, Baum and co-workers [5, 6, 7, 8]. The emphasis of this early work was to test the stability and consistency of the basic hydrodynamic solver, especially the velocity-pressure coupling that is vitally important in low Mach number applications. Many numerical algorithms developed up to that point in time were intended for use in high-speed flow applications, like aerospace. Many of the techniques adopted by FDS were originally developed for

---

<sup>1</sup>The National Institute of Standards and Technology (NIST) was formerly known as the National Bureau of Standards.

meteorological models, and as such needed to be tested to assess whether they would be appropriate to describe relatively low-speed flow within enclosures.

- A fundamental decision made by Rehm and Baum early in the FDS development was to use a direct (rather than iterative) solver for the pressure. In the low Mach number formulation of the Navier-Stokes equations, an elliptic partial differential equation for the pressure emerges, often referred to as the Poisson equation. Most CFD methods use iterative techniques to solve the governing conservation equations to avoid the necessity of directly solving the Poisson equation. The reason for this is that the equation is time-consuming to solve numerically on anything but a rectilinear grid. Because FDS is designed specifically for rectilinear grids, it can exploit fast, direct solvers of the Poisson equation, obtaining the pressure field with one pass through the solver to machine accuracy. FDS employs double-precision (8 byte) arithmetic, meaning that the relative difference between the computed and the exact solution of the discretized Poisson equation is on the order of  $10^{-12}$ . The fidelity of the numerical solution of the entire system of equations is tied to the pressure/velocity coupling because often simulations can involve hundreds of thousands of time steps, with each time step consisting of two solutions of the Poisson equation to preserve second-order accuracy. Without the use of the direct Poisson solver, build-up of numerical error over the course of a simulation could produce spurious results. Indeed, an attempt to use single-precision (4 byte) arithmetic to conserve machine memory led to spurious results simply because the error per time step built up to an intolerable level.

## 2.2 Numerical Tests

Numerical techniques used to solve the governing equations within a model can be a source of error in the predicted results. The hydrodynamic model within FDS is second-order accurate in space and time. This means that the error terms associated with the approximation of the spatial partial derivatives by finite differences is of the order of the square of the grid cell size, and likewise the error in the approximation of the temporal derivatives is of the order of the square of the time step. As the numerical grid is refined, the “discretization error” decreases, and a more faithful rendering of the flow field emerges. The issue of grid sensitivity is extremely important to the proper use of the model and will be taken up in the next chapter.

A common technique of testing flow solvers is to systematically refine the numerical grid until the computed solution does not change, at which point the calculation is referred to as a Direct Numerical Solution (DNS) of the governing equations. For most practical fire scenarios, DNS is not possible on conventional computers. However, FDS does have the option of running in DNS mode, where the Navier-Stokes equations are solved without the use of sub-grid scale turbulence models of any kind. Because the basic numerical method is the same for LES and DNS, DNS calculations are a very effective way to test the basic solver, especially in cases where the solution is steady-state. Throughout its development, FDS has been used in DNS mode for special applications. For example, FDS (or its core algorithms) have been used at a grid resolution of roughly 1 mm to look at flames spreading over paper in a microgravity environment [9, 10, 11, 12, 13, 14], as well as “g-jitter” effects aboard spacecraft [15]. Simulations have been compared to experiments performed aboard the US Space Shuttle. The flames are laminar and relatively simple in structure, and the comparisons are a qualitative assessment of the model solution. Similar studies have been performed comparing DNS simulations of a simple burner flame to laboratory experiments [16]. Another study compared FDS simulations of a counterflow diffusion flames to experimental measurements and the results of a one-dimensional multi-step kinetics model [17].

Early work with the hydrodynamic solver compared two-dimensional simulations of gravity currents with salt-water experiments [18]. In these tests, the numerical grid was systematically refined until almost perfect agreement with experiment was obtained. Such convergence would not be possible if there were a fundamental flaw in the hydrodynamic solver.



## 2.3 Sensitivity Analysis

A sensitivity analysis considers the extent to which uncertainty in model inputs influences model output. Model parameters can be the physical properties of solids and gases, boundary conditions, initial conditions, *etc.* The parameters can also be purely numerical, like the size of the numerical grid. FDS typically requires the user to provide several dozen different types of input parameters that describe the geometry, materials, combustion phenomena, *etc.* By design, the user is not expected to provide numerical parameters besides the grid size, although the optional numerical parameters are described in both the Technical Reference Guide and the User's Guide.

FDS does not limit the range of most of the input parameters because applications often push beyond the range for which the model has been validated. FDS is still used for research at NIST and elsewhere, and the developers do not presume to know in all cases what the acceptable range of any parameter is. Plus, FDS solves the fundamental conservation equations and is much less susceptible to errors resulting from input parameters that stray beyond the limits of simpler empirical models. However, the user is warned that he/she is responsible for the prescription of all parameters. The FDS manuals can only provide guidance.

The grid size is the most important numerical parameter in the model, as it dictates the spatial and temporal accuracy of the discretized partial differential equations. The heat release rate is the most important physical parameter, as it is the source term in the energy equation. Property data, like the thermal conductivity, density, heat of vaporization, heat capacity, *etc.*, ought to be assessed in terms of their influence on the heat release rate. Validation studies have shown that FDS predicts well the transport of heat and smoke when the HRR is prescribed. In such cases, minor changes in the properties of bounding surfaces do not have a significant impact on the results. However, when the HRR is not prescribed, but rather predicted by the model using the thermophysical properties of the fuels, the model output is sensitive to even minor changes in these properties.

The sensitivity analyses described in this chapter are all performed in basically the same way. For a given scenario, best estimates of all the relevant physical and numerical parameters are made, and a "baseline" simulation is performed. Then, one by one, parameters are varied by a given percentage, and the changes in predicted results are recorded. This is the simplest form of sensitivity analysis. More sophisticated techniques that involve the simultaneous variation of several parameters are impractical with a CFD model because the computation time is too long and the number of parameters too large to perform the necessary number of calculations to generate decent statistics.

### 2.3.1 Grid Sensitivity

The most important decision made by a model user is the size of the numerical grid. In general, the finer the numerical grid, the better the numerical solution of the equations. FDS is second-order accurate in space and time, meaning that halving the grid cell size will decrease the discretization error in the governing equations by a factor of 4. Because of the non-linearity of the equations, the decrease in discretization error does not necessarily translate into a comparable decrease in the error of a given FDS output quantity. To find out what effect a finer grid has on the solution, model users usually perform some form of grid sensitivity study in which the numerical grid is systematically refined until the output quantities do not change appreciably with each refinement. Of course, with each halving of the grid cell size, the time required for the simulation increases by a factor of  $2^4 = 16$  (a factor of two for each spatial coordinate, plus time). In the end, a compromise is struck between model accuracy and computer capacity.

Some grid sensitivity studies have been documented and published. Since FDS was first publicly released in 2000, significant changes in the combustion and radiation routines have been incorporated into the model. However, the basic transport algorithm is the same, as is the critical importance of grid sensitivity. In compiling sensitivity studies, only those that examined the sensitivity of routines no longer used have been

excluded.

As part of a project to evaluate the use of FDS version 1 for large scale mechanically ventilated enclosures, Friday [19] performed a sensitivity analysis to find the approximate calculation time based on varying grid sizes. A propylene fire with a nominal heat release rate was modeled in FDS. There was no mechanical ventilation and the fire was assumed to grow as a function of the time from ignition squared. The compartment was a 3 m by 3 m by 6.1 m space. Temperatures were sampled 12 cm below the ceiling. Four grid sizes were chosen for the analysis: 30 cm, 15 cm, 10 cm, 7.5 cm. Temperature estimates were not found to change dramatically with different grid dimensions.

Using FDS version 1, Bounagui *et al.* [20] studied the effect of grid size on simulation results to determine the nominal grid size for future work. A propane burner 0.1 m by 0.1 m was modeled with a heat release rate of 1500 kW. A similar analysis was performed using Alpert's ceiling jet correlation [21] that also showed better predictions with smaller grid sizes. In a related study, Bounagui *et al.* [22] used FDS to evaluate the emergency ventilation strategies in the Louis-Hippolyte-La Fontaine Tunnel in Montreal, Canada.

Xin [23] used FDS to model a methane fueled square burner (1 m by 1 m) in the open. Engineering correlations for plume centerline temperature and velocity profiles were compared with model predictions to assess the influence of the numerical grid and the size of the computational domain. The results showed that FDS is sensitive to grid size effects, especially in the region near the fuel surface, and domain size effects when the domain width is less than twice the plume width. FDS uses a constant pressure assumption at open boundaries. This assumption will affect the plume behavior if the boundary of the computational domain is too close to the plume.

Ierardi and Barnett [24] used FDS version 3 to model a 0.3 m square methane diffusion burner with heat release rate values in the range of 14.4 kW to 57.5 kW. The physical domain used was 0.6 m by 0.6 m with uniform grid spacings of 15, 10, 7.5, 5, 3, 1.5 cm for all three coordinate directions. For both fire sizes, a grid spacing of 1.5 cm was found to provide the best agreement when compared to McCaffrey's centerline plume temperature and velocity correlations [25]. Two similar scenarios that form the basis for Alpert's ceiling jet correlation were also modeled with FDS. The first scenario was a 1 m by 1 m, 670 kW ethanol fire under a 7 m high unconfined ceiling. The planar dimensions of the computational domain were 14 m by 14 m. Four uniform grid spacings of 50, 33.3, 25, and 20 cm were used in the modeling. The best agreement for maximum ceiling jet temperature was with the 33.3 cm grid spacing. The best agreement for maximum ceiling jet velocity was for the 50 cm grid spacing. The second scenario was a 0.6 m by 0.6 m 1000 kW ethanol fire under a 7.2 m high unconfined ceiling. The planar dimensions of the computational domain were 14.4 m by 14.4 m. Three uniform grid spacings of 60, 30, and 20 cm were used in the modeling. The results show that the 60 cm grid spacing exhibits the best agreement with the correlations for both maximum ceiling jet temperature and velocity on a qualitative basis.

Petterson [26] also completed work assessing the optimal grid size for FDS version 2. The FDS model predictions of varying grid sizes were compared to two separate fire experiments: The University of Canterbury McLeans Island Tests and the US Navy Hangar Tests in Hawaii. The first set of tests utilized a room with approximate dimensions of 2.4 m by 3.6 m by 2.4 m and fire sizes of 55 kW and 110 kW. The Navy Hangar tests were performed in a hangar measuring 98 m by 74 m by 15 m in height and had fires in the range of 5.5 MW to 6.6 MW. The results of this study indicate that FDS simulations with grids of 0.15 m had temperature predictions as accurate as models with grids as small as 0.10 m. Each of these grid sizes produced results within 15 % of the University of Canterbury temperature measurements. The 0.30 m grid produced less accurate results. For the comparison of the Navy Hangar tests, grid sizes ranging from 0.60 m to 1.80 m yielded results of comparable accuracy.

Musser *et al.* [27] investigated the use of FDS for course grid modeling of non-fire and fire scenarios. Determining the appropriate grid size was found to be especially important with respect to heat transfer at heated surfaces. The convective heat transfer from the heated surfaces was most accurate when the near

surface grid cells were smaller than the depth of the thermal boundary layer. However, a finer grid size produced better results at the expense of computational time. Accurate contaminant dispersal modeling required a significantly finer grid. The results of her study indicate that non-fire simulations can be completed more quickly than fire simulations because the time step is not limited by the large flow speeds in a fire plume.

### 2.3.2 Sensitivity of Large Eddy Simulation Parameters

FDS uses the Smagorinsky form of the Large Eddy Simulation (LES) technique. This means that instead of using the actual fluid viscosity, the model uses a viscosity of the form

$$\mu_{\text{LES}} = \rho (C_s \Delta)^2 |S| \quad (2.1)$$

where  $C_s$  is an empirical constant,  $\Delta$  is a length on the order of the size of a grid cell, and the deformation term  $|S|$  is related to the Dissipation Function (see FDS Technical Reference Guide [28] for details). Related to the “turbulent viscosity” are comparable expressions for the thermal conductivity and material diffusivity:

$$k_{\text{LES}} = \frac{\mu_{\text{LES}} c_p}{\text{Pr}_t} \quad ; \quad (\rho D)_{\text{LES}} = \frac{\mu_{\text{LES}}}{\text{Sc}_t} \quad (2.2)$$

where  $\text{Pr}_t$  and  $\text{Sc}_t$  are the turbulent Prandtl and Schmidt numbers, respectively. Thus,  $C_s$ ,  $\text{Pr}_t$  and  $\text{Sc}_t$  are a set of empirical constants. Most FDS users simply use the default values of (0.2,0.5,0.5), but some have explored their effect on the solution of the equations.

In an effort to validate FDS with some simple room temperature data, Zhang *et al.* [29] tried different combinations of the Smagorinsky parameters, and suggested the current default values. Of the three parameters, the Smagorinsky constant  $C_s$  is the most sensitive. Smagorinsky [30] originally proposed a value of 0.23, but researchers over the past three decades have used values ranging from 0.1 to 0.23. There are also refinements of the original Smagorinsky model [31, 32, 33] that do not require the user to prescribe the constants, but rather generate them automatically as part of the numerical scheme.

### 2.3.3 Sensitivity of Radiation Parameters

Radiative heat transfer is included in FDS via the solution of the radiation transport equation for a non-scattering gray gas, and in some limited cases using a wide band model. The equation is solved using a technique similar to finite volume methods for convective transport, thus the name given to it is the Finite Volume Method (FVM). There are several limitations of the model. First, the absorption coefficient for the smoke-laden gas is a complex function of its composition and temperature. Because of the simplified combustion model, the chemical composition of the smokey gases, especially the soot content, can effect both the absorption and emission of thermal radiation. Second, the radiation transport is discretized via approximately 100 solid angles. For targets far away from a localized source of radiation, like a growing fire, the discretization can lead to a non-uniform distribution of the radiant energy. This can be seen in the visualization of surface temperatures, where “hot spots” show the effect of the finite number of solid angles. The problem can be lessened by the inclusion of more solid angles, but at a price of longer computing times. In most cases, the radiative flux to far-field targets is not as important as those in the near-field, where coverage by the default number of angles is much better.

Hostikka *et al.* examined the sensitivity of the radiation solver to changes in the assumed soot production, number of spectral bands, number of control angles, and flame temperature. Some of the more interesting findings were:

- Changing the soot yield from 1 % to 2 % increased the radiative flux from a simulated methane burner about 15 %

- Lowering the soot yield to zero decreased the radiative flux about 20 %.
- Increasing the number of control angles by a factor of 3 was necessary to ensure the accuracy of the model at the discrete measurement locations.
- Changing the number of spectral bands from 6 to 10 did not have a strong effect on the results.
- Errors of 100 % in heat flux were caused by errors of 20 % in absolute temperature.

The sensitivity to flame temperature and soot composition are consistent with combustion theory, which states that the source term of the radiative transport equation is a function of the absorption coefficient multiplied by the absolute temperature raised to the fourth power. The number of control angles and spectral bands are user-controlled numerical parameters whose sensitivities ought to be checked for each new scenario. The default values in FDS are appropriate for most large scale fire scenarios, but may need to be refined for more detailed simulations such as a low-sooting methane burner.

### 2.3.4 Sensitivity of Thermophysical Properties of Solid Fuels

An extensive amount of verification and validation work with FDS version 4 has been performed by Hietaniemi, Hostikka, and Vaari at VTT, Finland [34]. The case studies are comprised of fire experiments ranging in scale from the cone calorimeter (ISO 5660-1) to full-scale fire tests such as the room corner test (ISO 9705). Comparisons are also made between FDS results and data obtained in the SBI (Single Burning Item) Euro-classification test apparatus (EN 13823) as well as data obtained in two *ad hoc* experimental configurations: one is similar to the room corner test but has only partial linings and the other is a space to study fires in building cavities.

All of the case studies involve real materials whose properties must be prescribed so as to conform to the assumption in FDS that solids are of uniform composition backed by a material that is either cold or totally insulating. Sensitivity of the various physical properties and the boundary conditions were tested. Some of the findings were:

- The measured burning rates of various materials often fell between two FDS predictions in which cold or insulated backings were assumed for the solid surfaces. FDS lacks a multi-layer solid model.
- The ignition time of upholstery is sensitive to the thermal properties of the fabric covering, but the steady burning rate is sensitive to the properties of the underlying foam.
- Moisture content of wooden fuels is very important and difficult to measure.
- Flame spread over complicated objects, like cables laid out in trays, can be modeled if the surface area of the simplified object is comparable to that of the real object. This suggests sensitivity not only to physical properties, but also geometry. It is difficult to quantify the extent of the geometrical sensitivity.

There is little quantification of the observed sensitivities in the study. Fire growth curves can be linear to exponential in form, and small changes in fuel properties can lead to order of magnitude changes in heat release rate for unconfined fires. The subject is discussed in the FDS Validation Guide (Volume 3 of the Technical Reference Guide), where it is noted in many of the studies that predicting fire growth is difficult.

Recently, Lautenberger, Rein and Fernandez-Pello [35] developed a method to automate the process of estimating material properties to input into FDS. The methodology involves simulating a bench-scale test with the model and iterating via a "genetic" algorithm to obtain an optimal set of material properties for that particular item. Such techniques are necessary because most bench-scale apparatus do not provide a complete set of thermal properties.

## 2.4 Code Checking

An examination of the structure of the computer program can be used to detect potential errors in the numerical solution of the governing equations. The coding can be verified by a third party either manually or automatically with profiling programs to detect irregularities and inconsistencies [2].

At NIST and elsewhere, FDS has been compiled and run on computers manufactured by IBM, Hewlett-Packard, Sun Microsystems, Digital Equipment Corporation, Apple, Silicon Graphics, Dell, Compaq, and various other personal computer vendors. The operating systems on these platforms include Unix, Linux, Microsoft Windows, and Mac OSX. Compilers used include Lahey Fortran, Digital Visual Fortran, Intel Fortran, IBM XL Fortran, HPUX Fortran, Forte Fortran for SunOS, the Portland Group Fortran, and several others. Each combination of hardware, operating system and compiler involves a slightly different set of compiler and run-time options and a rigorous evaluation of the source code to test its compliance with the Fortran 90 ISO/ANSI standard [36]. Through this process, out-dated and potentially harmful code is updated or eliminated, and often the code is streamlined to improve its optimization on the various machines. However, simply because the FDS source code can be compiled and run on a wide variety of platforms does not guarantee that the numerics are correct. It is only the starting point in the process because it at least rules out the possibility that erratic or spurious results are due to the platform on which the code is running.

Beyond hardware issues, there are several useful techniques for checking the FDS source code that have been developed over the years. One of the best ways is to exploit symmetry. FDS is filled with thousands of lines of code in which the partial derivatives in the conservation equations are approximated as finite differences. It is very easy in this process to make a mistake. Consider, for example, the finite difference approximation of the thermal diffusion term in the  $ijk$ th cell of the three-dimensional grid:

$$\begin{aligned}
 (\nabla \cdot k \nabla T)_{ijk} \approx & \frac{1}{\delta x} \left[ k_{i+\frac{1}{2},jk} \frac{T_{i+1,jk} - T_{ijk}}{\delta x} - k_{i-\frac{1}{2},jk} \frac{T_{ijk} - T_{i-1,jk}}{\delta x} \right] + \\
 & \frac{1}{\delta y} \left[ k_{i,j+\frac{1}{2},k} \frac{T_{i,j+1,k} - T_{ijk}}{\delta y} - k_{i,j-\frac{1}{2},k} \frac{T_{ijk} - T_{i,j-1,k}}{\delta y} \right] + \\
 & \frac{1}{\delta z} \left[ k_{ij,k+\frac{1}{2}} \frac{T_{ij,k+1} - T_{ijk}}{\delta z} - k_{ij,k-\frac{1}{2}} \frac{T_{ijk} - T_{ij,k-1}}{\delta z} \right]
 \end{aligned}$$

which is written as follows in the Fortran source code:

```

DTDX = (TMP(I+1,J,K)-TMP(I,J,K))*RDXN(I)
KDTDX(I,J,K) = .5*(KP(I+1,J,K)+KP(I,J,K))*DTDX
DTDY = (TMP(I,J+1,K)-TMP(I,J,K))*RDYN(J)
KDTDY(I,J,K) = .5*(KP(I,J+1,K)+KP(I,J,K))*DTDY
DTDZ = (TMP(I,J,K+1)-TMP(I,J,K))*RDZN(K)
KDTDZ(I,J,K) = .5*(KP(I,J,K+1)+KP(I,J,K))*DTDZ

DELKDELT = (KDTDX(I,J,K)-KDTDX(I-1,J,K))*RDX(I) +
.          (KDTDY(I,J,K)-KDTDY(I,J-1,K))*RDY(J) +
.          (KDTDZ(I,J,K)-KDTDZ(I,J,K-1))*RDZ(K)

```

This is one of the simpler constructs because the pattern that emerges within the lines of code make it fairly easy to check. However, a mis-typing of an  $I$  or a  $J$ , a plus or a minus sign, or any of a hundred different mistakes can cause the code to fail, or worse produce the wrong answer. A simple way to eliminate many of these mistakes is to run simple scenarios that have perfectly symmetric initial and boundary conditions. For example, put a hot cube in the exact center of a larger cold compartment, turn off gravity, and watch the heat diffuse from the hot cube into the cold gas. Any simple error in the coding of the energy equation will show

up almost immediately. Then, turn on gravity, and in the absence of any coding error, a perfectly symmetric plume will rise from the hot cube. This checks both the coding of the energy and the momentum equations. Similar checks can be made for all of the three dimensional finite difference routines. So extensive are these types of checks that the release version of FDS has a routine that generates a tiny amount of random noise in the initial flow field so as to eliminate any false symmetries that might arise in the numerical solution.

The process of adding new routines to FDS is as follows: typically the routine is written by one person (not necessarily a NIST staffer) who takes the latest version of the source code, adds the new routine, and writes a theoretical and numerical description for the FDS Technical Reference Guide, plus a description of the input parameters for the FDS User's Guide. The new version of FDS is then tested at NIST with a number of benchmark scenarios that exercise the range of the new parameters. Provisional acceptance of the new routine is based on several factors: (1) it produces more accurate results when compared to experimental measurement, (2) the theoretical description is sound, and (3) any empirical parameters are obtainable from the open literature or standard bench-scale apparatus. If the new routine is accepted, it is added to a test version of the software and evaluated by external users and/or NIST grantees whose research is related to the subject. Assuming that there are no intractable issues that arise during the testing period, the new routine eventually becomes part of the release version of FDS.

Even with all the code checking performed at NIST, it is still possible for errors to go unnoticed. One remedy is the fact that the source code for FDS is publicly released. Although it consists of on the order of 30,000 lines of Fortran statements, various researchers outside of NIST have been able to work with it, add enhancements needed for very specific applications or for research purposes, and report back to the developers bugs that have been detected. The source code is organized into 27 separate files, each containing subroutines related to a particular feature of the model, like the mass, momentum, and energy conservation equations, sprinkler activation and sprays, the pressure solver, *etc.* The lengthiest routines are devoted to input, output and initialization. Most of those working with the source code do not concern themselves with these lengthy routines but rather focus on the finite-difference algorithm contained in a few of the more important files. Most serious errors are found in these files, for they contain the core of the algorithm. The external researchers provide feedback on the organization of the code and its internal documentation, that is, comments within the source code itself. Plus, they must compile the code on their own computers, adding to its portability.

## Chapter 3

# The Basic Flow Solver

In this chapter we present test cases aimed at exercising the advective, pressure, and viscous terms, as well as the time integration for non-reacting flows.

### 3.1 2D Analytical Solution to Navier-Stokes

In this section we present an analytical solution that is useful for confirming the convergence rates of the truncation errors in the discretization of the terms in the governing equations. Consider the 2D incompressible Navier-Stokes equations

$$\frac{\partial \mathbf{u}}{\partial t} + \mathbf{u} \cdot \nabla \mathbf{u} = -\nabla p + \nu \nabla^2 \mathbf{u}, \quad (3.1)$$

where the velocity is given by  $\mathbf{u} = [u, v]^T$ , and the kinematic viscosity and pressure are denoted  $\nu$  and  $p$ , respectively. An analytical solution of these equations is given by [37]

$$u(x, y, t) = 1 - A \cos(x - t) \sin(y - t) e^{-2\nu t}, \quad (3.2)$$

$$v(x, y, t) = 1 + A \sin(x - t) \cos(y - t) e^{-2\nu t}, \quad (3.3)$$

$$p(x, y, t) = -\frac{A^2}{4} [\cos(2(x - t)) + \cos(2(y - t))] e^{-4\nu t}. \quad (3.4)$$

Here,  $A$  represents an arbitrary amplitude and is assumed to take a value of 2 in this example. Note that this solution satisfies continuity for all time,

$$\nabla \cdot \mathbf{u} = 0, \quad (3.5)$$

is spatially periodic on an interval  $2\pi$  in each direction, and is temporally periodic on  $2\pi$  if  $\nu = 0$ ; otherwise, the solution decays exponentially. Below we present two series of tests which demonstrate the second-order accuracy of the FDS numerical scheme and thus provide a strong form of code verification for the advective and viscous terms which are exercised.

The physical domain of the problem is a square of side  $L = 2\pi$ . The grid spacing is uniform  $\delta x = \delta y = L/N$  in each direction with  $N = \{8, 16, 32, 64\}$  for each test series. The staggered grid locations are denoted  $x_i = i\delta x$  and  $y_j = j\delta y$ , and the cell centers are marked by an overbar,  $\bar{x}_i = x_i - \delta x/2$  and  $\bar{y}_j = y_j - \delta y/2$ .

First, we present qualitative results for the case in which  $\nu = 0$ . Thus, only the advective discretization and the time integration are being tested. Figure 3.1 shows the initial and final ( $t = 2\pi$ ) numerical solution for the case  $N = 64$ . As mentioned, with  $\nu = 0$  the solution is periodic in time and this figure demonstrates that, as should be the case, the FDS numerical solution is unaltered after one flow-through time.

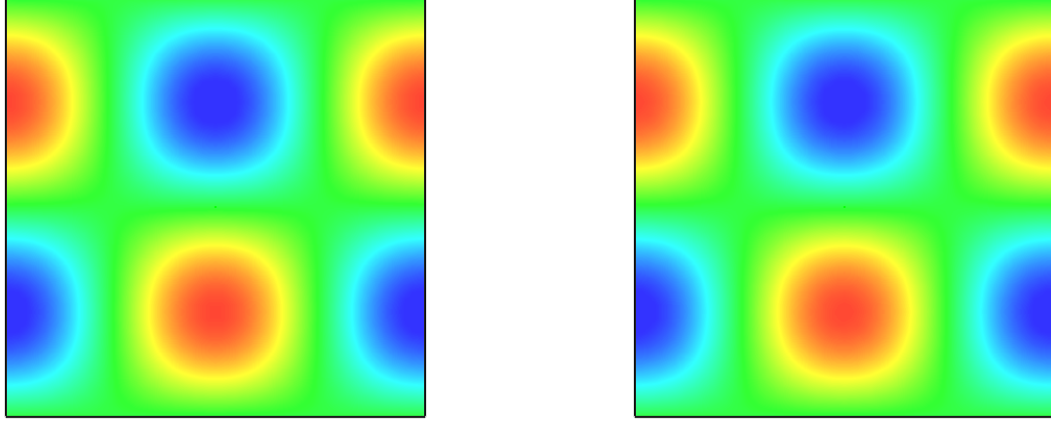


Figure 3.1: Initial and final states of the  $u$ -component of velocity.

Next, in Figure 3.2, we show time histories of the  $u$ -component of velocity at the center of the domain for the case in which  $v = 0.1$ . It is clearly seen that the FDS solution (thin line) converges to the analytical solution (thick line). Note that the analytical solution is evaluated at the same location as the FDS staggered grid location for the  $u$ -component of velocity,  $(x_{N/2}, \bar{y}_{N/2})$ , which is different in each case,  $N = \{8, 16, 32, 64\}$ .

Figure 3.3 is the key quantitative result of this verification test. In this figure we plot the rms error,  $\epsilon_{\text{rms}}$ , in the  $u$ -component of velocity against the grid spacing. The error is defined by

$$\epsilon_{\text{rms}} \equiv \sqrt{\frac{1}{M} \sum_{k=1}^M \left[ U_{ij}^k - u(x_i, \bar{y}_j, t_k) \right]^2}, \quad (3.6)$$

where  $M$  is the number of time steps and  $k$  is the time step index. The spatial indices are  $(i = N/2, j = N/2)$  and  $U_{ij}^k$  represents the FDS value for the  $u$ -component of velocity at the staggered storage location for cell  $(i, j)$  at time step  $k$ ;  $u(x_i, \bar{y}_j, t_k)$  is the analytical solution for the  $u$ -component at the corresponding location in space and time. The figure confirms that the advective terms, the viscous terms, and the time integration in the FDS code are convergent and second-order accurate.



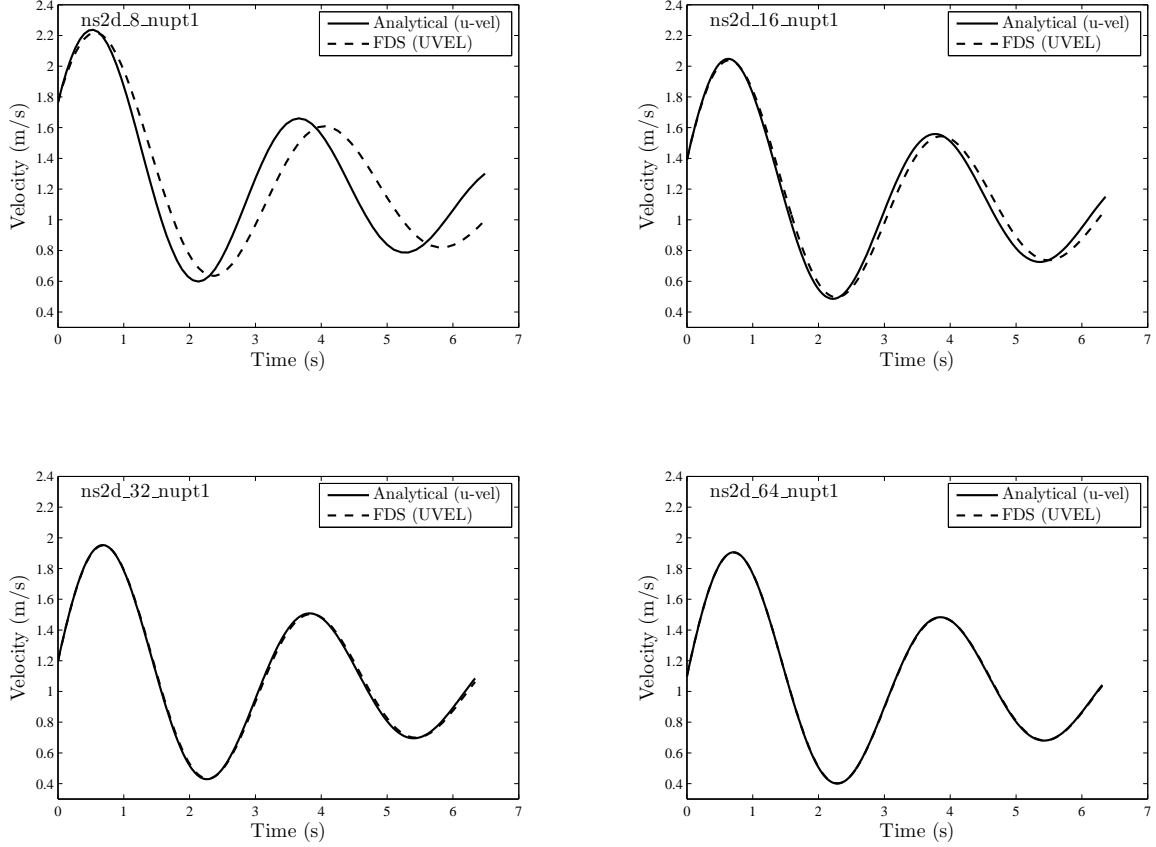


Figure 3.2: Time history of the  $u$ -component of velocity half a grid cell below the center of the domain for a range of grid resolutions. The domain is a square of side  $L = 2\pi$  m. The  $N \times N$  grid is uniform. Progressing from left to right and top to bottom we have resolutions  $N = \{8, 16, 32, 64\}$  clearly showing convergence of the FDS numerical solution (open circles) to the analytical solution (solid line). The case is run with constant properties,  $\rho = 1 \text{ kg/m}^3$  and  $\mu = 0.1 \text{ kg/m/s}$ , and a CFL of 0.25.

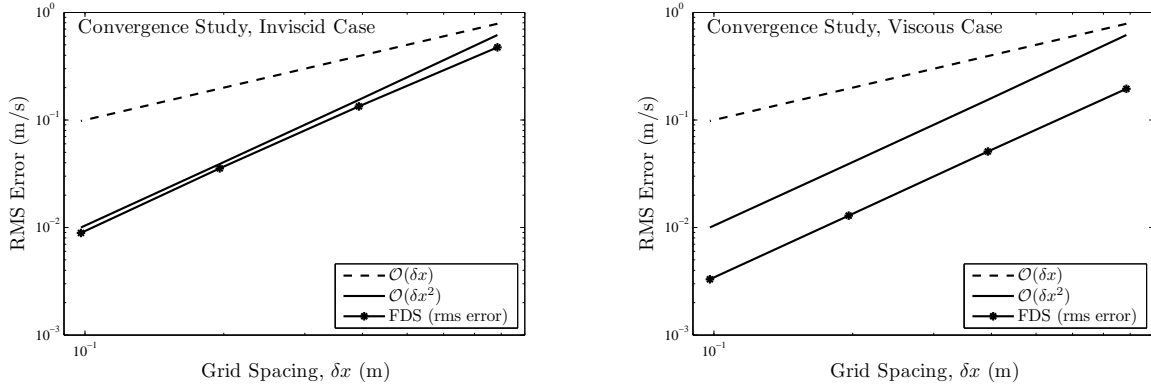


Figure 3.3: (Left) Convergence rate for the  $u$ -component of velocity with  $v = 0$  showing that the advective terms in the FDS code are second-order accurate. The triangles represent the rms error in the  $u$ -component for grid spacings of  $\delta x = L/N$  where  $L = 2\pi$  m and  $N = \{8, 16, 32, 64\}$ . The solid line represents first-order accuracy and the dashed line represents second-order accuracy. The simulation is run to a time of  $t = 2\pi$  s with a CFL of 0.25. The  $u$ -component at the center of the domain is compared with the analytical solution at the same location. (Right) Same case, except  $v = 0.1$ , showing that the viscous terms in the FDS code are second-order accurate.

## 3.2 Decaying Isotropic Turbulence

In this section we present a canonical flow for LES which tests whether the subgrid stress model has been coded properly. In some cases the difference between verification and validation is not so clear. Once a model is well-established and validated it may actually be used as a form of verification. Granted, such a test is not as strong a verification as the convergence study shown in Section 3.1. Nevertheless, these tests are often quite useful in discovering problems within the code. The case we examine in this section, decaying isotropic turbulence, is highly sensitive to errors in the advective and diffusive terms because the underlying physics is inherently three-dimensional and getting the problem right depends strongly on a delicate balance between vorticity dynamics and dissipation. An even more subtle yet extremely powerful verification test is also presented in this section when we set both the molecular and turbulent viscosities to zero and confirm that the integrated kinetic energy within the domain remains constant. In the absence of any form of viscosity, experience has shown that the slightest error in the advective terms or the pressure projection will cause the code to go unstable. This verification is therefore stronger than one might initially expect.

In this section we test the FDS model against the low Reynolds number (Re) data of Comte-Bellot and Corrsin (CBC) [38]. Viscous effects are important in this data set for a well-resolved LES, testing the model’s Re dependence. Following [39], we use a periodic box of side  $L = 9 \times 2\pi$  centimeters ( $\approx 0.566$  m) and  $\nu = 1.5 \times 10^{-5}$  m<sup>2</sup>/s for the kinematic viscosity. The non-dimensional times for this data set are:  $x/M = 42$  (initial condition), 98, and 171, where  $M$  is the characteristic mesh spacing of the CBC wind tunnel and  $x$  is the downstream location of the data station. Considering the mean velocity in the CBC wind tunnel experiment, these correspond to dimensional times of  $t = 0.00, 0.28$ , and  $0.66$  seconds in our simulations.

The initial condition for the FDS simulation is generated by superimposing Fourier modes with random phases such that the spectrum matches that of the initial CBC data. An iterative procedure is employed where the field is allowed to decay for small time increments subject to Navier-Stokes physics, each wavenumber is then injected with energy to again match the initial filtered CBC spectrum. The specific filter used here is discussed in [40].

To provide the reader with a qualitative sense of the flow, Figure 3.4 shows the initial and final states of the velocity field in the 3D periodic domain. The flow is unforced and so if viscosity is present the total energy decays with time due to viscous dissipation. Because the viscous scales are unresolved, a subgrid stress model is required. Here the stress is closed using the gradient diffusion hypothesis and the eddy viscosity is modeled by the constant coefficient Smagorinsky model with the coefficient taken to be  $C_s = 0.2$  (see the Technical Reference Guide for further details).

The decay curves for two grid resolutions are shown plotted on the left in Figure 3.5. For an LES code such as FDS which uses a physically-based subgrid model, an important verification test is to run this periodic isotropic turbulence simulation in the absence of both molecular and turbulent viscosity. For so-called “energy-conserving” explicit numerics the integrated energy will remain nearly constant in time. This is demonstrated by the blue line in the top-left plot in Figure 3.5. The deviations from identical energy conservation (to machine precision) are due solely to the time discretization (the spatial terms are conservative as discussed in [41]) and converge to zero as the time step goes to the zero. Note that strict energy conservation requires implicit time integration [42, 43] and, as shown by the red curve on the same plot where only molecular viscosity is present in the simulation, this cost is unwarranted given that the molecular dissipation rate clearly overshadows the relatively insignificant amount of numerical dissipation caused by the explicit method. The FDS result using the Smagorinsky eddy viscosity (the black solid line) matches the CBC data (red open circles) well for the  $32^3$  case (top-left). However, the FDS results are slightly too dissipative in the  $64^3$  case (bottom-left). This is due to a well-known limitation of the constant coefficient Smagorinsky model: namely, that the eddy viscosity does not converge to zero at the appropriate rate as the filter width

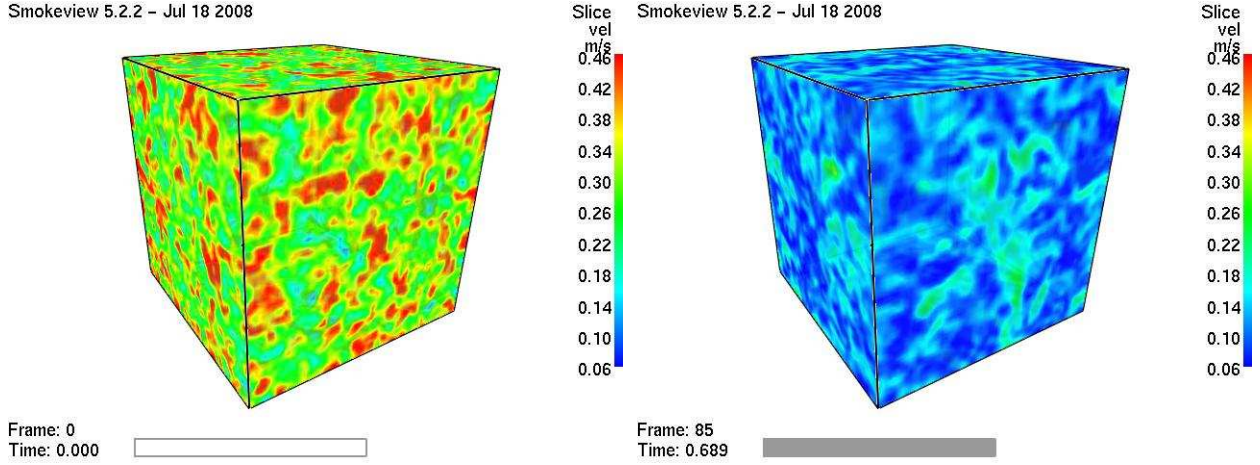


Figure 3.4: Initial and final states of the isotropic turbulence field.

(here equivalent to the grid spacing) is decreased.

To the right of each decay curve plot in Figure 3.5 is the corresponding spectral data comparison. The three black solid lines are the CBC spectral data for the points in time corresponding to dimensional times of  $t = 0.00$ ,  $0.28$ , and  $0.66$  seconds in our simulations. As described above, the initial FDS velocity field (represented by the black dots) is specified to match the CBC data up to the grid Nyquist limit. From there the spectral energy decays rapidly as discussed in [40]. For each of the spectral plots on the right, the results of interest are the values of the red and blue dots and how well these match up with the corresponding CBC data. For the  $32^3$  case (top-right) the results are remarkably good. Interestingly, the results for the more highly resolved  $64^3$  case are not as good. This is because the viscous scales are rather well-resolved at the later times in the experiment and, as mentioned, it is well-known that the constant coefficient Smagorinsky model is too dissipative under such conditions.

Overall, the agreement between the FDS simulations and the CBC data is satisfactory and any discrepancies can be explained by limitations of the model. Therefore, as a verification the results here are positive in that nothing points to coding errors.

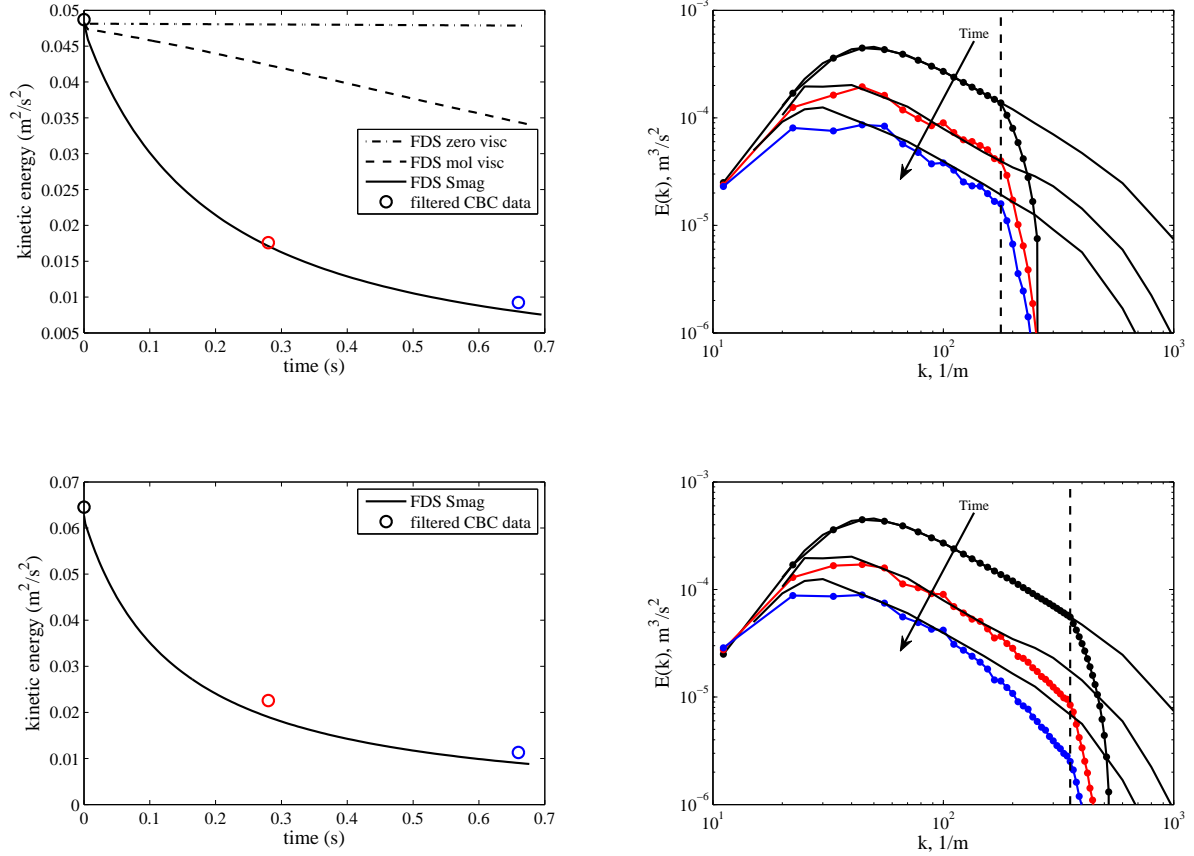


Figure 3.5: (Left) Time histories of integrated kinetic energy corresponding to the grid resolutions on the right side of the figure. In the  $32^3$  case (top), the CBC data (open circles) are obtained by applying a filter to the CBC energy spectra at the Nyquist limit for an  $N = 32$  grid. Similarly, for the  $64^3$  case (bottom), the CBC data are obtained from filtered spectra for an  $N = 64$  grid. Notice that the integrated FDS results for the  $32^3$  case compare better with the filtered CBC data than the  $64^3$  results. This is a well-known limitation of the constant coefficient Smagorinsky model: namely, that the eddy viscosity does not converge to zero at the appropriate rate as the filter width (here equivalent to the grid spacing) is decreased. (Right) Energy spectra for the  $32^3$  case (top) and the  $64^3$  case (bottom). The solid black lines are the spectral data of Comte-Bellot and Corrsin at three different points in time corresponding to downstream positions in the turbulent wind tunnel. The initial condition for the velocity field (spectra shown as black dots) in the FDS simulation is prescribed such that the energy spectrum matches the initial CBC data. The FDS energy spectra corresponding to the subsequent CBC data are shown by the red and blue dots. The vertical dashed line represents the wavenumber of the grid Nyquist limit.

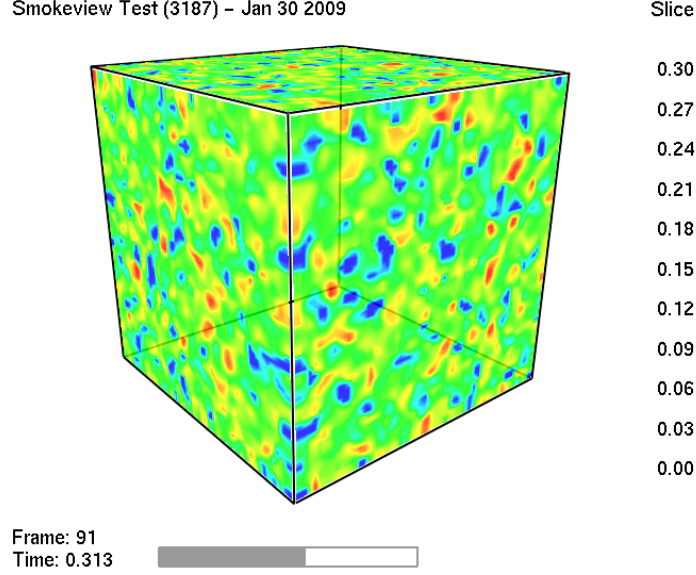


Figure 3.6: Smagorinsky coefficient for a  $64^3$  simulation of the CBC experiment.

### 3.3 The Dynamic Smagorinsky Model

In the previous section, all calculations were performed with a constant and uniform Smagorinsky coefficient,  $C_s = 0.2$ . For the canonical case of homogeneous decaying isotropic turbulence – *at sufficiently high Reynolds number* – this model is sufficient. However, we noticed that, even for the isotropic turbulence problem, when the grid Reynolds number is low (i.e., the flow is well-resolved) the constant coefficient model tends to over predict the dissipation of kinetic energy (see Figure 3.5). This is because the eddy viscosity does not converge to zero at the proper rate; so long as strain is present in the flow (the magnitude of the strain rate tensor is nonzero), the eddy viscosity will be nonzero. This violates a guiding principle in LES development: that the method should converge to a DNS if the flow field is sufficiently resolved [44].

The dynamic procedure for calculating the model coefficient (invoked by setting `DYNMAG = .TRUE.` on the `MISC` line) alleviates this problem. The basis of the model is that the coefficient should be the same for two different filter scales within the inertial subrange. Details of the procedure are explained in the following references [45, 46, 47, 48, 49]. Here we present results for the implementation of the dynamic model in FDS. In Figure 3.6 we show contours of the Smagorinsky coefficient  $C_s(\mathbf{x}, t)$  at a time midway through a  $64^3$  simulation of the CBC experiment. Notice that the coefficient ranges from 0.00 to roughly 0.30 within the domain with the average value falling around 0.17.

Next, in Figure 3.7, we show results for the dynamic model analogous to Figure 3.5. For the  $32^3$  case the result is not dramatically different than the constant coefficient model. In fact, one might argue that the  $32^3$  constant coefficient results are slightly better. But there are several reasons why we should not stop here and conclude that the constant coefficient model is superior. First, as pointed out in Pope Exercise 13.34 [50],  $38^3$  is required to resolve 80% of the total kinetic energy (for this flow) and thus put the cutoff wavenumber within the inertial subrange of turbulent length scales. Pope recommends that simulations which are under-resolved by this criterion should be termed “very large-eddy simulations” – weather forecasting is a typical example. For a  $32^3$  LES, the test filter width in the dynamic model falls at a resolution of  $16^3$ , clearly outside the inertial range. A tacit assumption underlying the original interpretation of the dynamic model is that both the grid filter scale and the test filter scale should fall within the inertial range, since this is the

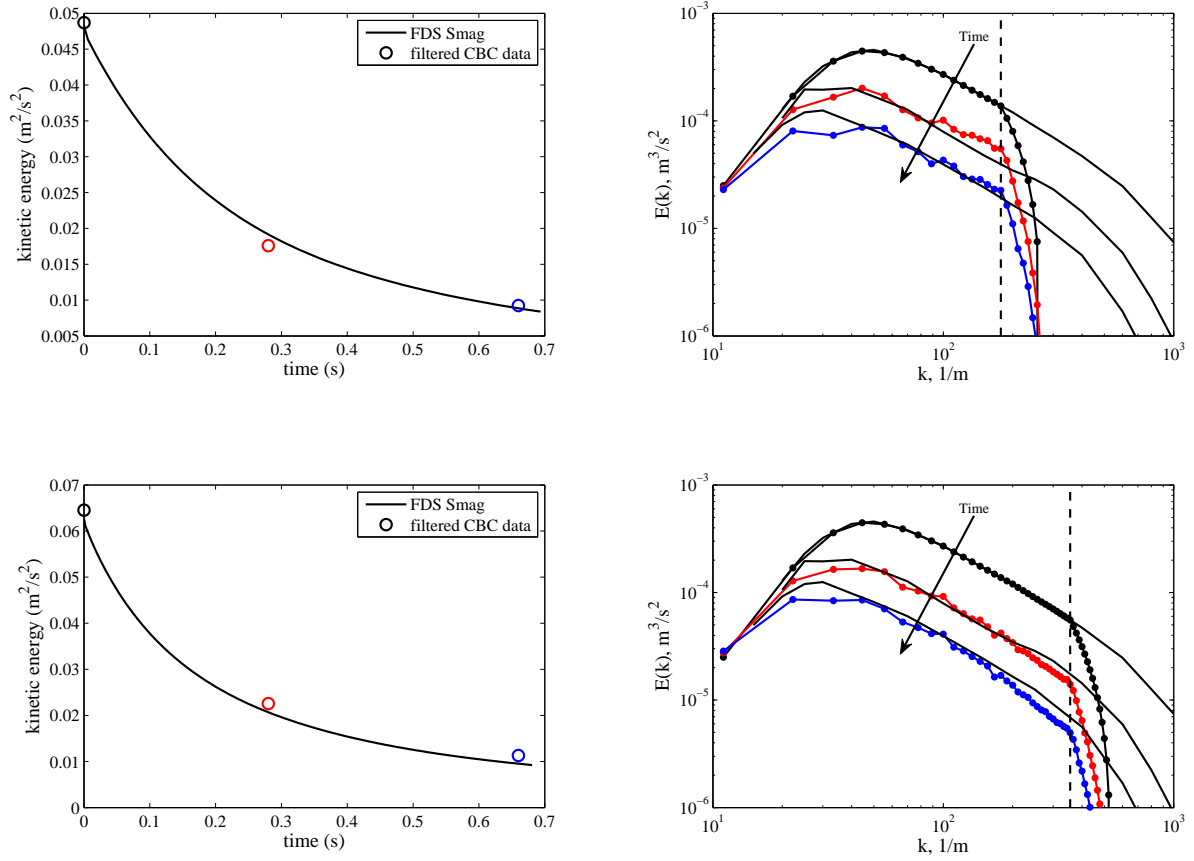


Figure 3.7: Dynamic Smagorinsky model results (analogous to Figure 3.5) for integrated kinetic energy (left) and spectra (right).

range in which the scales of turbulent motion (in theory) exhibit fractal-like, scale similar behavior (recently the procedure has been derived from other arguments [51]). With this in mind, it is perhaps not surprising that the dynamic model does not perform optimally for the low resolution case. In the higher resolution  $64^3$  case, however, the dynamic model does perform better than the constant coefficient model – and this is the desired result: we want better performance at higher resolution. As can be seen from the energy spectra (lower right), the energy near the grid Nyquist limit is more accurately retained by the dynamic model. This equates to better flow structure with fewer grid cells. Thus, for practical calculations of engineering interest the small computational overhead of computing the coefficient may be recuperated by a reduction in cell count.

### 3.4 FDS Wall Flows Part I: Straight Channels

Wall flows are notoriously challenging for large-eddy simulation (LES) [52, 53, 54, 50, 55]. In spite of their promise and sophistication, practical LES codes are resigned to *model* the wall shear stress as opposed to *resolving* the dynamically important length scales near the wall.

In this work we introduce the Werner and Wengle (WW) wall model [56] into the NIST Fire Dynamics Simulator (FDS) as a practical first step in developing models for turbulent flow around complex geometry and over complex terrain. Such models are required in order for FDS to accurately model, for example, tunnel fires, smoke transport in complex architectures, and wildland-urban interface (WUI) fires [57]. As a minimum requirement, a wall model should accurately reproduce the mean wall stress for flow in a straight channel. We verify that this is true for FDS by reproducing the Moody chart, a plot of friction factor versus Reynolds number for pipe flow [58].

The remainder of this article is organized as follows. In Section 3.4.1 we describe the model formulation. In Section 3.4.2 we give an overview of the WW model. Then, in Section 3.4.3, we conduct a verification study of the wall boundary conditions for laminar and turbulent flows in FDS. From this study we are able to draw quantitative conclusions in Section 3.4.4 about the accuracy of the channel flow simulations.

#### 3.4.1 Formulation

Details of the FDS formulation are given in the Technical Guide [59]. Here we provide only the salient components of the model necessary for treatment of constant density channel flow.

The filtered continuity and momentum equations are:

$$\frac{\partial \bar{u}_i}{\partial x_i} = 0, \quad (3.7)$$

$$\frac{\partial \bar{u}_i}{\partial t} + \frac{\partial \bar{u}_i \bar{u}_j}{\partial x_j} = -\frac{1}{\rho} \left[ \frac{dp}{dx_i} + \frac{\partial \bar{p}}{\partial x_i} + \frac{\partial \bar{\tau}_{ij}}{\partial x_j} + \frac{\partial \tau_{ij}^{sgs}}{\partial x_j} \right], \quad (3.8)$$

where  $\tau_{ij}^{sgs} \equiv \rho(\bar{u_i u_j} - \bar{u}_i \bar{u}_j)$  is the subgrid-scale (sgs) stress tensor, here modeled by gradient diffusion with dynamic Smagorinsky [45] used for the eddy viscosity. In this work we specify a constant pressure drop  $dp/dx$  in the streamwise direction to drive the flow. The hydrodynamic pressure  $\bar{p}$  is obtained from a Poisson equation which enforces (3.7).

When (3.8) is integrated over a cell adjacent to the wall in an LES it turns out that the most difficult term to handle is the viscous stress at the wall, e.g.  $\bar{\tau}_{xz}|_{z=0}$ , because the wall-normal gradient of the streamwise velocity component cannot be resolved. Note that the sgs stress at the wall is identically zero. We have, therefore, an entirely different situation than exists in the bulk flow at high Reynolds number where the viscous terms are negligible and the sgs stress is of critical importance. The quality of the sgs model still influences the wall stress, however, since other components of the sgs tensor affect the value of the near-wall velocity and hence the resulting viscous stress determined by the wall model. In particular, it is important that the sgs model is *convergent* (in the sense that the LES formulation reduces to a DNS as the filter width becomes small) so that as the grid is refined we can expect more accurate results from the simulation.

The model used for  $\tau_w = \bar{\tau}_{xz}|_{z=0}$  in this work is the Werner and Wengle model [56] which we describe in more detail below.

#### 3.4.2 The Werner and Wengle Wall Model

An important scaling quantity in the near-wall region is the friction velocity, defined as  $u^* \equiv \sqrt{\tau_w/\rho}$ . From the friction velocity we define the nondimensional streamwise velocity  $u^+ \equiv u/u^*$  and nondimensional wall-



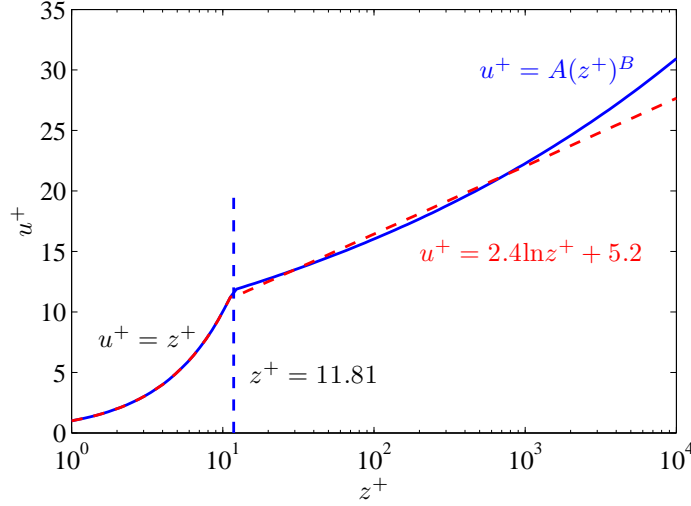


Figure 3.8: The law of the wall. We have omitted the buffer layer since it is not considered in the WW model. For  $z^+ \leq 11.81$  we have the viscous sublayer. For  $z^+ > 11.81$  we show a comparison of the log law (3.10) (red dashed line) and the WW power law (3.12) (blue solid line) with  $A = 8.3$  and  $B = 1/7$ .

normal distance  $z^+ \equiv z/\ell$ , where  $\ell = \mu/(\rho u^*)$ . The law of the wall is then given by [50, 60]

$$u^+ = z^+ \quad \text{for } z^+ < 5, \quad (3.9)$$

$$u^+ = 2.4 \ln z^+ + 5.2 \quad \text{for } z^+ > 30, \quad (3.10)$$

The region  $5 < z^+ < 30$ , where both viscous and inertial stresses are important, is referred to as the buffer layer. The upper range of the log law depends on the Reynolds number [50, 61].

Werner and Wengle [56] propose a simplification to the law of the wall to eliminate the mathematical difficulties of handling the buffer and log layers. Furthermore, WW suppose that their simplified formula for the streamwise velocity holds *instantaneously* within the LES. The WW wall law is [55]

$$u^+ = z^+ \quad \text{for } z^+ \leq 11.81, \quad (3.11)$$

$$u^+ = A(z^+)^B \quad \text{for } z^+ > 11.81, \quad (3.12)$$

where  $A = 8.3$  and  $B = 1/7$ . Note that a power law has been substituted for the log law and the viscous sublayer and the power law region are matched within the buffer region. A comparison of the log law and the power law is shown in Figure 3.8. In the region  $11.81 < z^+ < 10^3$  the power law is a good approximation to the log law and for  $z^+ > 10^3$  the power law loosely exhibits wake region behavior for a flow with  $\text{Re} \approx 5e5$  [50, 61]. As we see below, this functional behavior has consequences for high Re flows.

For the purposes of adapting the WW model to FDS we suppose that the first off-wall velocity component  $\tilde{u}$  represents the WW profile averaged in the wall-normal direction (refer to Figure 3.9). The density is taken as the average of the neighboring cell values and uniform along the face. The WW model as implemented in FDS is then given by

$$|\tau_w| = \frac{2\bar{\mu}|\tilde{u}|}{\Delta z} \quad \text{for } z^+ \leq 11.81, \quad (3.13)$$

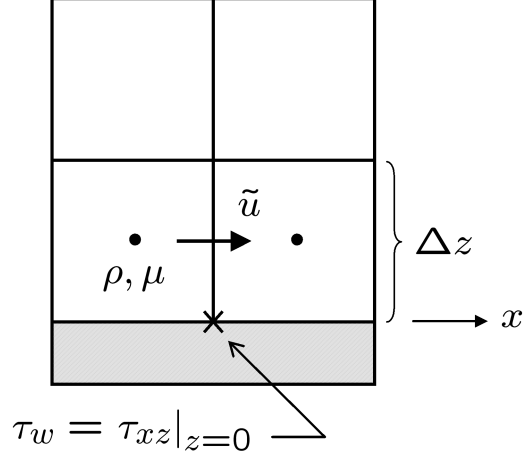


Figure 3.9: Near-wall grid.

$$|\tau_w| = \bar{\rho} \left[ \alpha \left( \frac{\bar{\mu}}{\bar{\rho} \Delta z} \right)^\beta + \eta \left( \frac{\bar{\mu}}{\bar{\rho} \Delta z} \right)^B |\tilde{u}| \right]^\gamma \quad \text{for } z^+ > 11.81, \quad (3.14)$$

where

$$\begin{aligned} \alpha &= \frac{1-B}{2} A^{\frac{1+B}{1-B}} \\ \beta &= 1+B \\ \eta &= \frac{1+B}{A} \\ \gamma &= \frac{2}{1+B} \end{aligned}$$

Note that  $\bar{\mu}$  is the average of the *molecular* viscosity from the neighboring cells.

In order to decide which formula to use for the wall stress, (3.13) or (3.14), we must know  $z^+$ , which of course depends on  $\tau_w$ . As a practical matter of implementation, given that most boundary layers in FDS are under-resolved, we first calculate  $\tau_w$  from (3.14); we then obtain  $z^+ = \sqrt{\tau_w / \bar{\rho}}$ ; if  $z^+ > 11.81$ , then the computed value of  $\tau_w$  is retained, else  $\tau_w$  is taken from (3.13), which actually involves no additional computation since the ghost cell value for the velocity is prescribed for a no-slip wall by default.

### 3.4.3 Results

#### Laminar

As verification of the no-slip boundary condition and further verification of the momentum solver in FDS, we perform a simple 2D laminar (Poiseuille) flow calculation of flow through a straight channel. The FDS input files are stored in the repository [62] under `poiseuille_*`. The height of the channel is  $H = 1$  m and the length of the channel is  $L = 8$  m. The number of grid cells in the streamwise direction  $x$  is  $N_x = 8$ . The number of cells in the wall-normal direction  $z$  is varied  $N_z = \{8, 16, 32, 64\}$ . The fluid density is  $\rho = 1.2$  kg m<sup>-3</sup> and the viscosity is 0.025 kg m<sup>-1</sup> s<sup>-1</sup>. The mean pressure drop is prescribed to be  $dp/dx = -1$  Pa m<sup>-1</sup> resulting in  $Re_H \approx 160$ . The (Moody) friction factor  $f$ , which satisfies

$$\Delta p = f \frac{L}{H} \frac{1}{2} \rho \bar{u}^2, \quad (3.15)$$

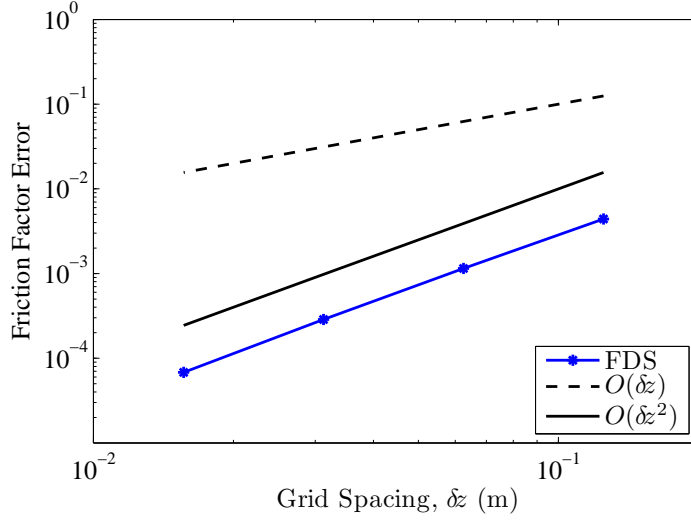


Figure 3.10: FDS exhibits second-order convergence for laminar (Poiseuille) flow in a 2D channel.

is determined from the steady state mean velocity  $\bar{u}$  which is output by FDS for the specified pressure drop. The exact friction factor for this flow is  $f_{exact} = 24/\text{Re}_H$ . The friction factor error  $|f - f_{exact}|$  is plotted for a range of grid spacings  $\delta z = H/N_z$  in Figure 3.10 demonstrating second-order convergence of the laminar velocity field.

### Turbulent

To verify the WW wall model for turbulent flow we perform 3D LES of a square channel with periodic boundaries in the streamwise direction and a constant and uniform mean pressure gradient driving the flow. The problem set up is nearly identical to the laminar cases of the previous section except here we perform 3D calculations and maintain cubic cells as we refine the grid: we hold the ratio 8:1:1 between  $N_x:N_y:N_z$  for all cases. The cases shown below are identified by their grid resolution in the  $z$  direction. The velocity field is initially at rest and develops in time to a mean steady state driven by the specified mean pressure gradient. The presence of a steady state is the result of a balance between the streamwise pressure drop and the integrated wall stress from the WW model. FDS outputs the planar average velocity in the streamwise direction and once a steady state is reached this value is used to compute the Reynolds number and the friction factor. Table 3.1 provides a case matrix: nine cases for three values of specified pressure drop and three grid resolutions. The nominal Reynolds number (obtained post-run) is listed along with the friction factor from the most refined FDS case and the friction factor computed (iteratively) from the Colebrook equation,

$$\frac{1}{\sqrt{f}} = -2.0 \log_{10} \left( \frac{\epsilon/D}{3.7} + \frac{2.51}{\text{Re}\sqrt{f}} \right), \quad (3.16)$$

which is a fit to the turbulent range of the Moody chart (see e.g. [63]). The parameter  $\epsilon/D$  is the relative roughness where  $D$  is the hydraulic diameter of the pipe or channel and  $\text{Re}$  is the Reynolds number based on  $D$ . For all the cases reported here the hydraulic diameter is equivalent to the channel height,  $D = H$ , and the walls of the channel are smooth, i.e.  $\epsilon = 0$ . FDS input files are stored in the repository [62] as `moody_*`.

Table 3.1: Case matrix and friction factor results for turbulent channel flow. The height of the first grid cell  $\Delta z$  is given in viscous units  $z^+$  for each case. Additionally, the table gives the nominal Reynolds number  $Re_H$  and the FDS friction factor results compared to the Colebrook equation (3.16).

$dp/dx$	$z^+$			$Re_H$	$f$ FDS	$f$ Colebrook	rel. error
(Pa/m)	$N_z = 8$	$N_z = 16$	$N_z = 32$		( $N_z = 32$ )	Eq. (3.16)	%
-0.01	190	95	47	$5.9 \times 10^4$	0.0212	0.0202	4.8
-1.	$1.9 \times 10^3$	950	470	$7.5 \times 10^5$	0.0128	0.0122	4.6
-100.	$1.9 \times 10^4$	$9.5 \times 10^3$	$4.7 \times 10^3$	$9.8 \times 10^6$	0.0077	0.0081	6.0

To provide a qualitative picture of the flow field, Figure 3.11 shows contours of streamwise velocity for the case  $dp/dx = -1 \text{ Pa m}^{-1}$  and  $N_z = 32$ .

In Figure 3.12 we replicate the Moody diagram for both the laminar and turbulent cases presented in this work. The laminar cases provide the exact result for two different Reynolds numbers and the turbulent cases are converging to the empirical values of the friction factor for smooth pipes. It is interesting to compare the turbulent results in Figure 3.12 with the values of  $z^+$  shown in Table 3.1. Notice from the table that the  $z^+$  values for the  $dp/dx = -100$  cases are in a range where the power law (3.12) deviates significantly from the log law (3.10) (see Figure 3.8) and this may explain why the results for this high Re case are somewhat grid sensitive.

### 3.4.4 Conclusions

In this work we have verified the FDS wall model for both laminar and turbulent flow through straight channels. We have shown that for the laminar (DNS) case FDS is second-order accurate. It is suggested elsewhere that, as a rule of thumb, 10 % accuracy is the best that can be expected from friction factor calculations of turbulent flow [63]. We have adapted the Werner and Wengle wall model to variable density flows (though only constant density flows are tested here) for smooth walls and have shown that, when combined with the dynamic model for the eddy viscosity, FDS is capable of reproducing friction factors for a broad range of Reynolds numbers to within 6.0 % relative accuracy.

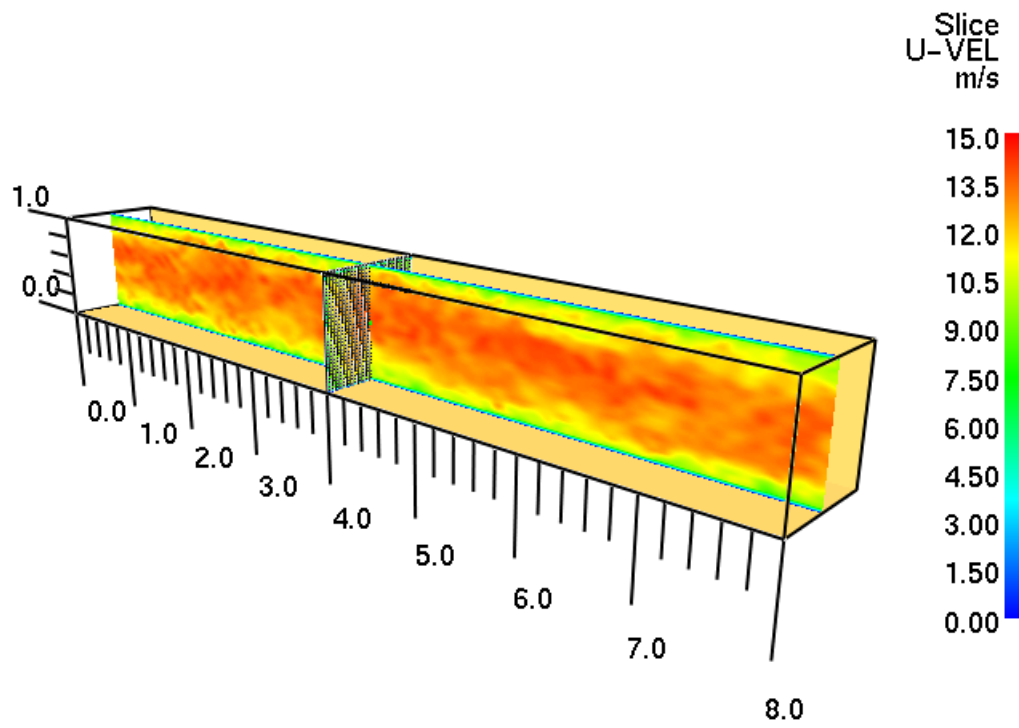


Figure 3.11: LES of square channel flow with smooth walls and periodic streamwise boundaries using dynamic Smagorinsky and the Werner Wengle wall model. For this image  $N_z = 32$  and the mean pressure drop is  $dp/dx = -1 \text{ Pa m}^{-1}$  resulting in  $Re_H = 7.5 \times 10^5$  and a friction factor of  $f = 0.0128$ .

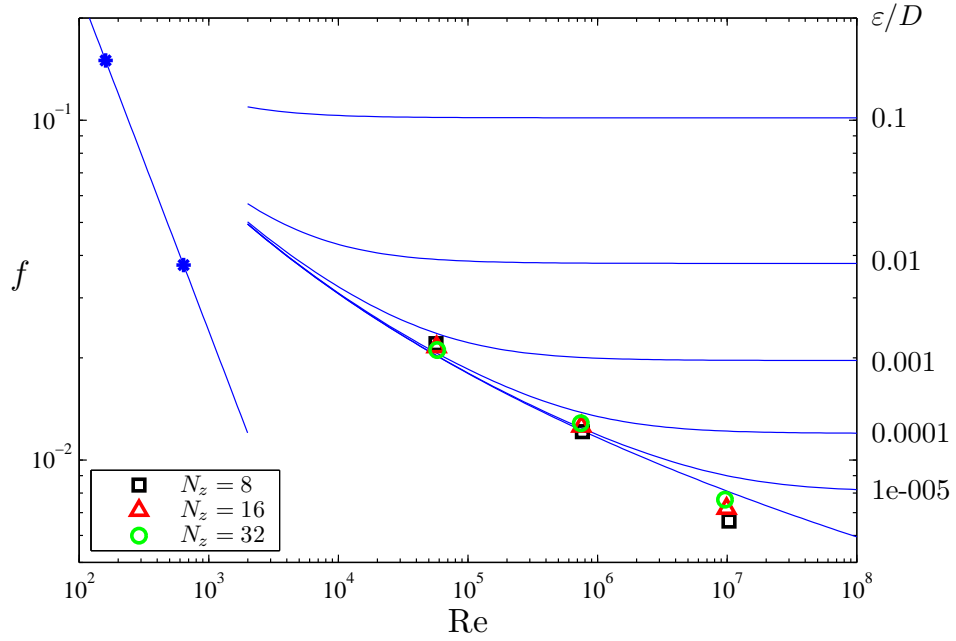


Figure 3.12: The FDS Moody Chart: friction factor,  $f$ , versus Reynolds number,  $Re$ . The solid line for  $Re < 2000$  is the analytical result for 2D Poiseuille flow,  $f = 24/Re$ . The solid lines for  $Re > 2000$  (from the Colebrook equation (3.16)) are for turbulent flow at various levels of relative roughness  $\varepsilon/D$  shown on the right axis. Stars are DNS results from FDS at a single grid resolution ( $N_z = 64$ ) and the symbols are FDS results for 3D LES with dynamic Smagorinsky and the Werner Wengle wall model at three grid resolutions ( $N_z = \{8, 16, 32\}$ ).

## Chapter 4

# Thermal Radiation

The Radiative Transport Equation (RTE) for an absorbing/emitting and scattering medium is

$$\mathbf{s} \cdot \nabla I_\lambda(\mathbf{x}, \mathbf{s}) = - \left[ \kappa(\mathbf{x}, \lambda) + \sigma_s(\mathbf{x}, \lambda) \right] I_\lambda(\mathbf{x}, \mathbf{s}) + B(\mathbf{x}, \lambda) + \frac{\sigma_s(\mathbf{x}, \lambda)}{4\pi} \int_{4\pi} \Phi(\mathbf{s}, \mathbf{s}') I_\lambda(\mathbf{x}, \mathbf{s}') d\mathbf{s}' \quad (4.1)$$

where  $I_\lambda(\mathbf{x}, \mathbf{s})$  is the radiation intensity at wavelength  $\lambda$ ,  $\mathbf{s}$  is the direction vector of the intensity,  $\kappa(\mathbf{x}, \lambda)$  and  $\sigma_s(\mathbf{x}, \lambda)$  are the local absorption and scattering coefficients, respectively, and  $B(\mathbf{x}, \lambda)$  is the emission source term. The integral on the right hand side describes the in-scattering from other directions. In the case of a non-scattering gas the RTE becomes

$$\mathbf{s} \cdot \nabla I_\lambda(\mathbf{x}, \mathbf{s}) = \kappa(\mathbf{x}, \lambda) \left[ I_b(\mathbf{x}) - I_\lambda(\mathbf{x}, \mathbf{s}) \right] \quad (4.2)$$

where  $I_b(\mathbf{x})$  is the source term given by the Planck function (see below).

In practical simulations the spectral ( $\lambda$ ) dependence cannot be solved accurately. Instead, the radiation spectrum is divided into a relatively small number of bands and a separate RTE is derived for each band. The band specific RTE is

$$\mathbf{s} \cdot \nabla I_n(\mathbf{x}, \mathbf{s}) = \kappa_n(\mathbf{x}) \left[ I_{b,n}(\mathbf{x}) - I_n(\mathbf{x}, \mathbf{s}) \right], \quad n = 1 \dots N \quad (4.3)$$

where  $I_n$  is the intensity integrated over the band  $n$ , and  $\kappa_n$  is the appropriate mean absorption coefficient inside the band. The source term can be written as a fraction of the blackbody radiation

$$I_{b,n} = F_n(\lambda_{\min}, \lambda_{\max}) \sigma T^4 / \pi \quad (4.4)$$

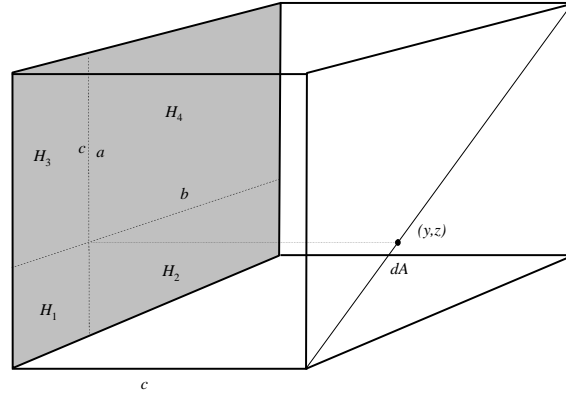
where  $\sigma$  is the Stefan-Boltzmann constant. The calculation of factors  $F_n$  is explained in Ref. [64]. When the intensities corresponding to the bands are known, the total intensity is calculated by summing over all the bands

$$I(\mathbf{x}, \mathbf{s}) = \sum_{n=1}^N I_n(\mathbf{x}, \mathbf{s}) \quad (4.5)$$

There are numerous examples in the heat transfer literature of exact solutions, for simple configurations of hot and cold objects, of the radiation transport equation.

## 4.1 Radiation inside a box (radiation\_in\_a\_box)

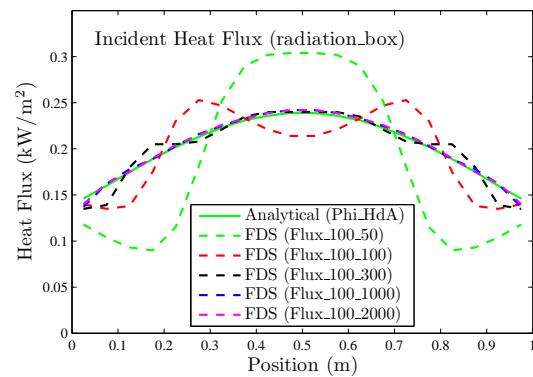
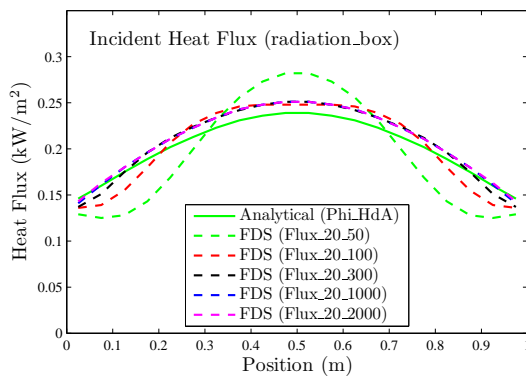
This verification case tests the computation of three-dimensional configuration factor  $\Phi$  inside a cube box with one hot wall and five cold (0 K) walls. An overview of the test geometry is shown here:



The configuration factors are calculated at the diagonal of the cold wall opposite to the hot wall. The exact values of the configuration factor from plane element  $dA$  to parallel rectangle  $H$  are calculated using the analytical solution [64]

(y,z)	$\Phi_{HdA}$	(y,z)	$\Phi_{HdA}$
0.025	0.1457	0.275	0.2135
0.075	0.1603	0.325	0.2233
0.125	0.1748	0.375	0.2311
0.175	0.1888	0.425	0.2364
0.225	0.2018	0.475	0.2391

Different variations of the case include the mesh resolution ( $20^3$  and  $100^3$  cells) and the number of radiation angles (50, 100, 300, 1000, 2000). The exact and FDS results are shown here:





## 4.2 Radiation from a plane layer (radiation\_plane\_layer)

This case tests the computation of three-dimensional radiation from a homogenous, infinitely wide layer of hot gases. The temperature of the layer is 1273.15 K and the absorption coefficient,  $\kappa$ , is varied. The thickness of the layer is fixed at 1 m, and the optical depth is  $\tau = (1 \kappa) \text{ m}^{-1}$ . Wall temperatures are set to 0 K. The results are compared against the exact solution  $S(\tau)$  presented in [65]

$$S(\tau) = S_b [1 - 2E_3(\tau)] \quad (4.6)$$

where  $S_b = \sigma T^4$  is the black-body heat flux from the radiating plane and  $E_3(\tau)$  is the exponential integral function (order 3) of the optical depth  $\tau$ .

The FDS results are computed at two mesh resolutions in the  $x$ -direction ( $I=20$  and  $I=150$ ). For  $I=20$ , both one-band and six-band versions are included to test the correct integration of heat fluxes over multiple bands. For  $I=20$ , 2-D versions are also computed ( $J=1$ ). The limiting case,  $\tau = \infty$ , using a solid wall of temperature 1273.15 K, is computed to test the wall heat flux computation. The exact values and FDS predictions of the wall heat fluxes are given in the table below.

$\tau$ ( $\text{m}^{-1}$ )	$S(\tau)$ ( $\text{kW/m}^2$ )	FDS ( $I=20, J=20$ )		FDS ( $I=20, J=1$ )		FDS ( $I=150$ )
		1 band	6 bands	1 band	6 bands	1 band
0.01	2.8970	2.9214	2.9104	2.8364	2.8257	2.9285
0.1	24.9403	25.5668	25.4705	25.1078	25.0133	25.7191
0.5	82.9457	83.1353	82.8224	84.3719	84.0542	84.0311
1.0	116.2891	115.4055	114.9711	117.8011	117.3576	116.7755
10	148.9698	148.9619	148.4011	148.9677	148.4069	148.9695
$\infty$	148.9709	147.7533	147.1970	147.9426	147.3856	147.9419

### 4.3 Wall Internal Radiation (wall\_internal\_radiation)

In-depth absorption of thermal radiation in a solid is computed using a two-flux model. In this example, the accuracy of the two-flux model is tested in the computation of the emissive flux from a 0.10 m thick, homogenous layer of material at a temperature of 1273.15 K surrounded by an ambient temperature of 10 K. The absorption coefficient is varied to cover a range [0.01, 10] of optical depth,  $\tau$ .

The exact solutions for radiative flux are the analytical solutions of plane layer emission [65]

$$S(\tau) = S_b [1 - 2E_3(\tau)] \quad (4.7)$$

where  $S_b = \sigma T^4$  is the black-body heat flux from the radiating plane and  $E_3(\tau)$  is the exponential integral function (order 3) of optical depth,  $\tau$ . The exact solutions and FDS results are shown in the table below.

$\tau$ (m <sup>-1</sup> )	$S(\tau)$ (kW/m <sup>2</sup> )	FDS (kW/m <sup>2</sup> )
0.01	2.897	2.950
0.1	24.94	26.98
0.5	82.95	93.90
1.0	116.3	128.4
10.	149.0	149.0

## Chapter 5

# Heat Conduction

This chapter contains examples that test the one-dimensional heat conduction solver in FDS. A one-dimensional heat conduction equation for the solid phase temperature  $T_s(x, t)$  is applied in the direction  $x$  pointing into the solid (the point  $x = 0$  represents the surface)

$$\rho_s c_s \frac{\partial T_s}{\partial t} = \frac{\partial}{\partial x} k_s \frac{\partial T_s}{\partial x} + \dot{q}_s''' \quad (5.1)$$

In cylindrical and spherical coordinates, the heat conduction equation is written

$$\rho_s c_s \frac{\partial T_s}{\partial t} = \frac{1}{r} \frac{\partial}{\partial r} \left( r k_s \frac{\partial T_s}{\partial r} \right) + \dot{q}_s''' \quad ; \quad \rho_s c_s \frac{\partial T_s}{\partial t} = \frac{1}{r^2} \frac{\partial}{\partial r} \left( r^2 k_s \frac{\partial T_s}{\partial r} \right) + \dot{q}_s''' \quad (5.2)$$

FDS offers the user these options, with the assumption that the obstruction is not actually recti-linear, but rather cylindrical or spherical in shape. This option is useful in describing the behavior of small, complicated “targets” like cables or heat detection devices.

## 5.1 Simple Heat Conduction Through a Solid Slab (heat\_conduction)

Analytical solutions of transient, one-dimensional heat conduction through a slab can be found in Refs. [66] and [67]. Four cases are examined here. In each, a slab of thickness  $L = 0.1$  m is exposed on one face to an air temperature of  $T_g = 120$  °C. The other face is insulated (adiabatic). The convective heat transfer from the gas to the slab is  $\dot{q}_c'' = h(T_g - T_s)$ , where  $h$  is constant, and  $T_s$  is the slab face temperature. No thermal radiation is included.

Case	$k$ (W/m/K)	$\rho$ (kg/m <sup>3</sup> )	$c$ (kJ/kg/K)	$h$ (W/m <sup>2</sup> /K)	Bi $hL/k$
A	0.1	100	1	100	100
B	0.1	100	1	10	10
C	1.0	1000	1	10	1
D	10.0	10000	1	10	0.1

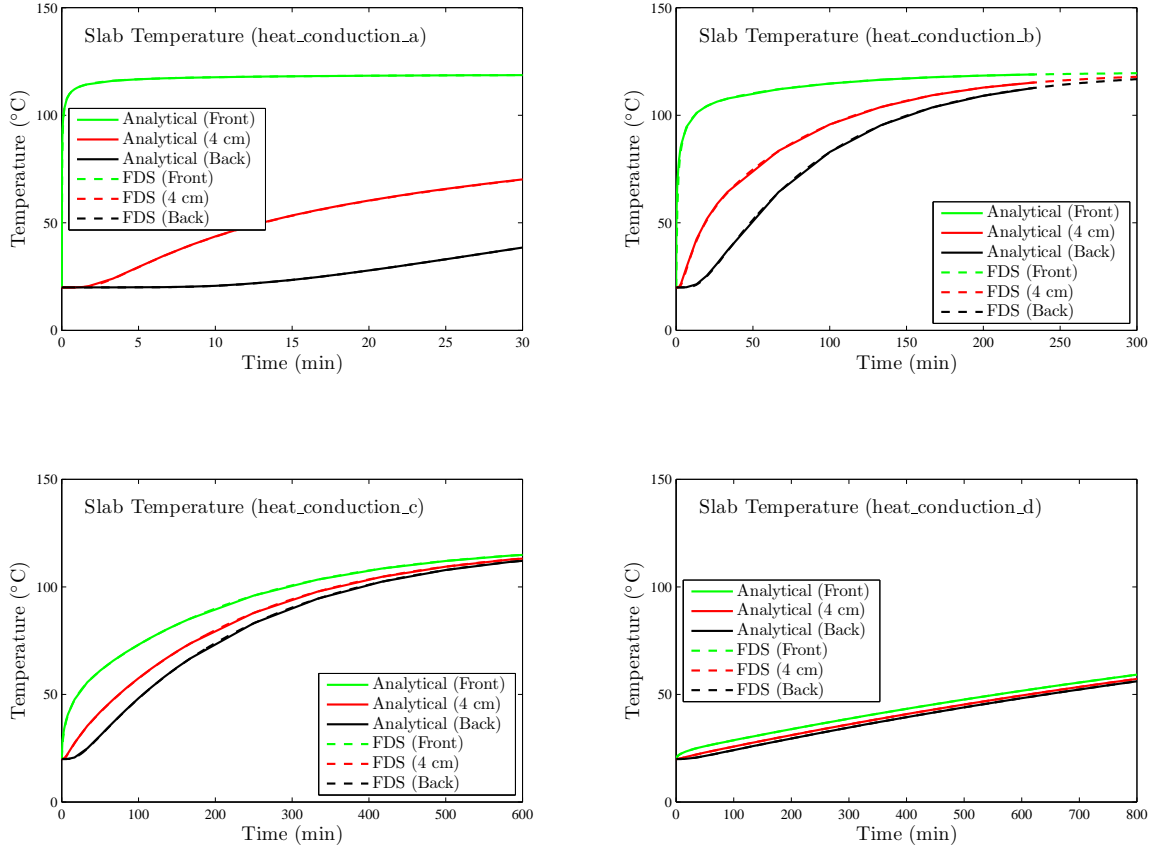


Figure 5.1: Comparison of heat conduction calculations with analytical solutions.

## 5.2 Temperature-Dependent Thermal Properties (heat\_conduction\_kc)

This example demonstrates the 1-D heat conduction in cartesian, cylindrical and spherical geometries with temperature-dependent thermal properties. The cartesian solution was computed using HEATING (version 7.3), a multi-dimensional, finite-difference, general purpose heat transfer model [68]. The cylindrical and spherical solutions were computed using a commercial finite-element solver, ABAQUS.

The sample of homogenous material is initially at 0 °C and at  $t > 0$  exposed to a gas at 700 °C. A fixed heat transfer coefficient of 10 W/m<sup>2</sup>/K is assumed. The density of the material is 10000 kg/m<sup>3</sup>. The conductivity and specific heat are functions of temperature with the following values:  $k(0) = 0.10$  W/m/K,  $k(200) = 0.20$  W/m/K,  $c(0) = 1.0$  kJ/kg/K,  $c(100) = 1.2$  kJ/kg/K,  $c(200) = 1.0$  kJ/kg/K. The thickness (radius) of the sample is 0.01 m. In the cartesian case, the back surface of the material is exposed to a gas at 0 °C. In the figure below, the light colored solid lines are FDS results and the dark lines are the HEATING results. An example input with cylindrical geometry looks like:

```
&MATL ID='MAT_1'
    EMISSIVITY = 0.0
    CONDUCTIVITY_RAMP='K_RAMP'
    SPECIFIC_HEAT_RAMP = 'C_RAMP'
    DENSITY=10000. /

&RAMP ID = 'K_RAMP' T=0,    F= 0.10 /
&RAMP ID = 'K_RAMP' T=100,  F= 0.15 /
&RAMP ID = 'K_RAMP' T=200,  F= 0.20 /
&RAMP ID = 'C_RAMP' T=0,    F= 1.00 /
&RAMP ID = 'C_RAMP' T=100,  F= 1.20 /
&RAMP ID = 'C_RAMP' T=200,  F= 1.00 /

&SURF ID='SLAB'
    STRETCH_FACTOR = 1.0
    GEOMETRY = 'CYLINDRICAL'
    MATL_ID='MAT_1'
    THICKNESS=0.01 /
```

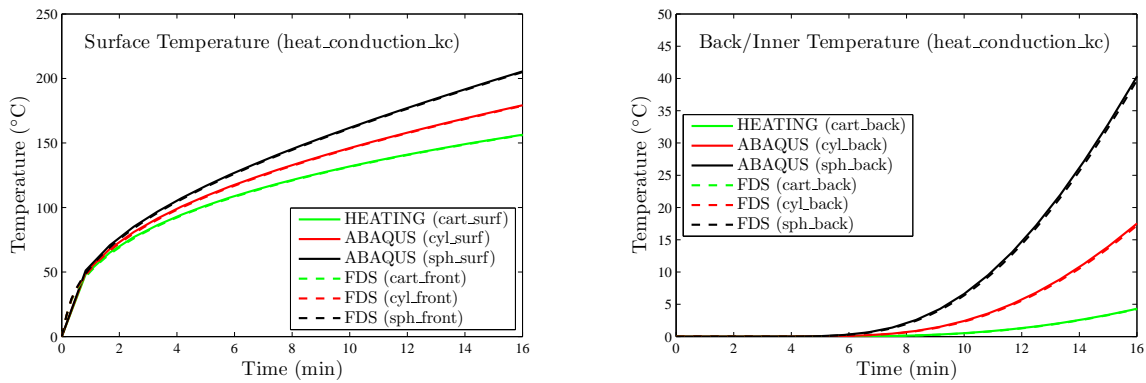


Figure 5.2: Comparison of heat conduction calculations with a finite-element model.



## Chapter 6

# Pyrolysis

Solids can undergo simultaneous reactions under the following assumptions:

- instantaneous release of volatiles from solid to the gas phase,
- local thermal equilibrium between the solid and the volatiles,
- no condensation of gaseous products, and
- no porosity effects

Each material component may undergo several competing reactions, and each of these reactions may produce some other solid component (residue), gaseous fuel, and/or water vapor according to the yield coefficients  $v_s$ ,  $v_f$  and  $v_w$ , respectively. These coefficients should usually satisfy  $v_s + v_f + v_w = 1$ , but smaller yields may also be used to take into account the gaseous products that are not explicitly included in the simulation.

## 6.1 A Simple Two-Step Pyrolysis Example (two\_step\_solid\_reaction)

Consider the set of ordinary differential equations describing the mass fraction of three components of a solid material undergoing thermal degradation:

$$\begin{aligned}\frac{dY_a}{dt} &= -K_{ab}Y_a \\ \frac{dY_b}{dt} &= K_{ab}Y_a - K_{bc}Y_b \\ \frac{dY_c}{dt} &= K_{bc}Y_b\end{aligned}\tag{6.1}$$

where the mass fraction of component  $a$  is 1 initially. The analytical solution is:

$$\begin{aligned}Y_a(t) &= \exp(-K_{ab}t) \\ Y_b(t) &= \frac{K_{ab}}{K_{bc} - K_{ab}} \exp(-K_{ab}t) - \exp(-K_{bc}t) \\ Y_c(t) &= [K_{ab}(1 - \exp(-K_{bc}t)) + K_{bc} * (\exp(-K_{ab}t) - 1)] / (K_{ab} - K_{bc})\end{aligned}\tag{6.2}$$

$$Y_c(t) = [K_{ab}(1 - \exp(-K_{bc}t)) + K_{bc} * (\exp(-K_{ab}t) - 1)] / (K_{ab} - K_{bc})\tag{6.3}$$

The analytical and numerical solution for the parameters  $K_{ab} = 0.389$  and  $K_{bc} = 0.262$  are shown here:

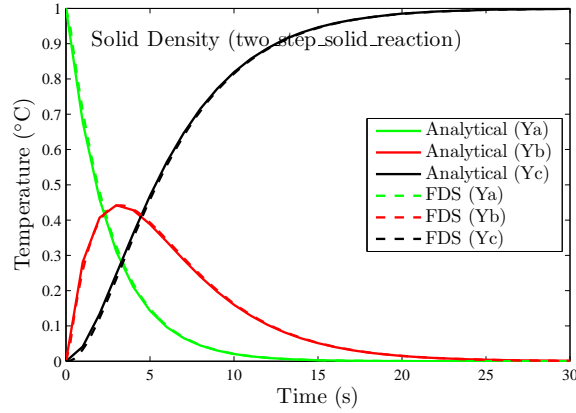


Figure 6.1: Comparison of a two-step solid pyrolysis calculation with an analytical solution.



## 6.2 Development of surface emissivity (emissivity)

For thermally thick surfaces, the surface emissivity is computed as a mass-weighted sum of the individual material emissivities in the first condensed phase grid cell. In the verification test, the initial material, having emissivity of 1.0, is converted to another material, having emissivity of 0.0, at a constant rate of  $0.1 \text{ s}^{-1}$ . As a result, the surface emissivity should change linearly from 1.0 to 0.0 in 10 s.

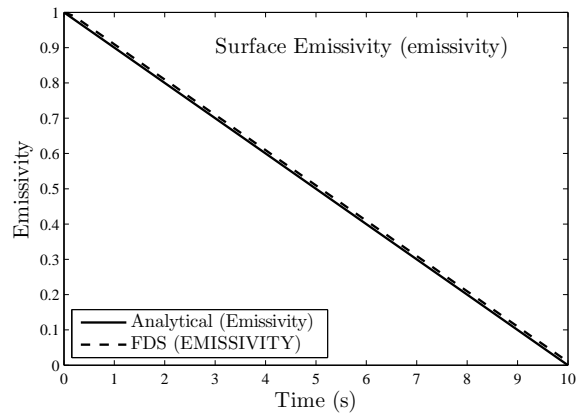


Figure 6.2: Testing the emissivity of solid materials.

### 6.3 Enthalpy of solid materials (enthalpy)

Consider a thin plate of conductive material that is exposed on one side to an elevated temperature heat source and exposed on the other to an ambient temperature void. In the thermally-thin limit, the temperature of the slab is governed by the following equation

$$\frac{dT_s}{dt} = \frac{\dot{q}_{\text{front}}'' + \dot{q}_{\text{back}}''}{c_s \rho_s \delta} \quad (6.4)$$

In this example, the initial exposure to the front side of the slab is  $3 \text{ kW/m}^2$ . The original material (call it A) undergoes a reaction to form material B. The reaction rate is constant,  $0.2 \text{ s}^{-1}$ , which in this case means that material A disappears in exactly 5 s. This is achieved by setting  $n_s$  and  $E$  to 0 and  $A$  to 0.2 in the reaction rate term:

$$r = \left( \frac{\rho_{s,A}}{\rho_{s0}} \right)^{n_s} A \exp \left( -\frac{E}{RT_s} \right) \quad (6.5)$$

The density and conductivity of both materials are  $30 \text{ kg/m}^3$  and  $10 \text{ W/m/K}$ , respectively. The emissivity of front and back is 1. The specific heat of material A changes from  $1.0 \text{ kJ/kg/K}$  to  $0.1 \text{ kJ/kg/K}$  above  $80^\circ \text{C}$ , while the specific heat of material B is constant at  $1.0 \text{ kJ/kg/K}$ . The slab is  $1 \text{ mm}$  thick.

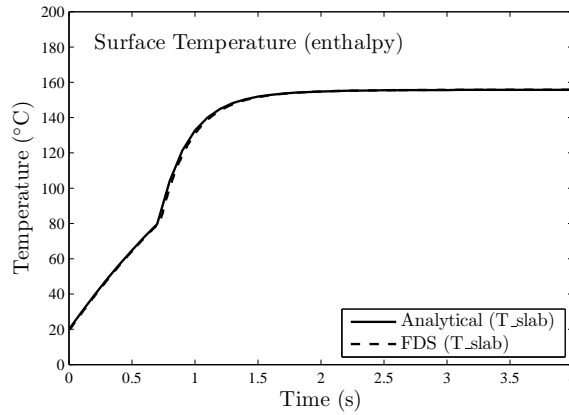


Figure 6.3: Testing the enthalpy of solid materials.

Note that the “analytical” solution is actually a simple numerical integration of the equations above with a small time step to ensure accuracy. This example tests a number of features, including the reaction rate, mass weighted specific heats, and radiation boundary conditions. Note that the convective heat transfer has been turned off, and the correct steady-state temperature is calculated by FDS.

## 6.4 Using TGA Data (birch\_tga)

This is an example of a comparison of a candidate solid phase model with TGA (Thermo-gravimetric Analysis) data. The sample cases called **birch\_tga\_1step\_2** and **birch\_tga\_1step\_20** simulate two standard TGA experiments in which small samples of birch wood are heated up slowly at constant rates of 2 °C/min and 20 °C/min, respectively. The model of the wood only involves one reaction that converts virgin wood to char and fuel gases. There is also a reaction in the simulation that does nothing more than evaporate the small amount of moisture in the wood. This evaporation is evident in Fig. 6.4 near the temperature of 100 °C.

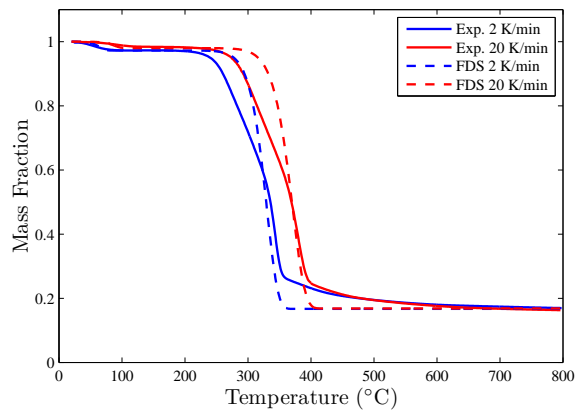


Figure 6.4: Comparison of a solid phase model of birch wood with TGA data.



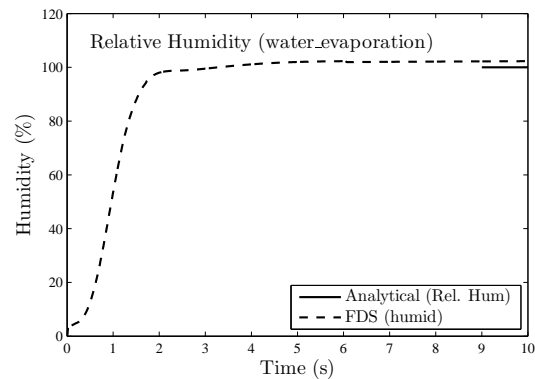
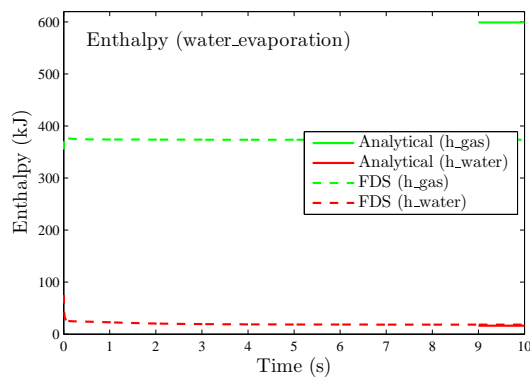
## Chapter 7

# Droplets

### 7.1 Water Droplet Evaporation (water\_evaporation)

The test case called **water\_evaporation** involves stationary water droplets in a box with dimensions of 1 m on a side. The walls of the box are assumed adiabatic. The air within the box is stirred to maintain uniform conditions, and there are no leaks or heat losses. Initially, the air temperature is 20 °C, the median volumetric diameter of the droplets is 100  $\mu\text{m}$ , the water temperature is 90 °C, and the total mass of water droplets is 0.2 kg. It is expected that a steady-state will be achieved after about 10 s. The initial energy content, the sum of the enthalpy of the water and air, is 75.3 kJ + 540.1 kJ = 615.4 kJ. After a short period of time, 0.0246 kg of water evaporates, the mass fraction of water vapor rises to 0.0205 kg/kg, and the air temperature increases to 22.3 °C. At this point the energy content of the water droplets and humid air is 16.2 kJ + 604.9 kJ = 621.1 kJ.

At 22.3 °C, the expected mass fraction of water vapor is 0.0201 kg/kg, but the predicted value is 0.0205 kg/kg, an over-prediction of about 2 %. The energy gained by the air is over-predicted by about 8 %.





# Bibliography

- [1] K.B. McGrattan, S. Hostikka, and J.E. Floyd. Fire Dynamics Simulator (Version 5), User's Guide. NIST Special Publication 1019-5, National Institute of Standards and Technology, Gaithersburg, Maryland, October 2007. [i](#)
- [2] American Society for Testing and Materials, West Conshohocken, Pennsylvania. *ASTM E 1355-04, Standard Guide for Evaluating the Predictive Capabilities of Deterministic Fire Models*, 2004. [i](#), [1](#), [9](#)
- [3] W. Mell, K.B. McGrattan, and H. Baum. Numerical Simulation of Combustion in Fire Plumes. In *Twenty-Sixth Symposium (International) on Combustion*, pages 1523–1530. Combustion Institute, Pittsburgh, Pennsylvania, 1996. [3](#)
- [4] K.B. McGrattan, H.R. Baum, and R.G. Rehm. Large Eddy Simulations of Smoke Movement. *Fire Safety Journal*, 30:161–178, 1998. [3](#)
- [5] H.R. Baum, R.G. Rehm, P.D. Barnett, and D.M. Corley. Finite Difference Calculations of Buoyant Convection in an Enclosure, Part I: The Basic Algorithm. *SIAM Journal of Scientific and Statistical Computing*, 4(1):117–135, March 1983. [3](#)
- [6] H.R. Baum and R.G. Rehm. Finite Difference Solutions for Internal Waves in Enclosures. *SIAM Journal of Scientific and Statistical Computing*, 5(4):958–977, December 1984. [3](#)
- [7] H.R. Baum and R.G. Rehm. Calculations of Three Dimensional Buoyant Plumes in Enclosures. *Combustion Science and Technology*, 40:55–77, 1984. [3](#)
- [8] R.G. Rehm, P.D. Barnett, H.R. Baum, and D.M. Corley. Finite Difference Calculations of Buoyant Convection in an Enclosure: Verification of the Nonlinear Algorithm. *Applied Numerical Mathematics*, 1:515–529, 1985. [3](#)
- [9] K.B. McGrattan, T. Kashiwagi, H.R. Baum, and S.L. Olson. Effects of Ignition and Wind on the Transition to Flame Spread in a Microgravity Environment. *Combustion and Flame*, 106:377–391, 1996. [4](#)
- [10] T. Kashiwagi, K.B. McGrattan, S.L. Olson, O. Fujita, M. Kikuchi, and K. Ito. Effects of Slow Wind on Localized Radiative Ignition and Transition to Flame Spread in Microgravity. In *Twenty-Sixth Symposium (International) on Combustion*, pages 1345–1352. Combustion Institute, Pittsburgh, Pennsylvania, 1996. [4](#)
- [11] W. Mell and T. Kashiwagi. Dimensional Effects on the Transition from Ignition to Flame Spread in Microgravity. In *Twenty-Seventh Symposium (International) on Combustion*, pages 2635–2641. Combustion Institute, Pittsburgh, Pennsylvania, 1998. [4](#)

- [12] W. Mell, S.L. Olson, and T. Kashiwagi. Flame Spread Along Free Edges of Thermally-Thin Samples in Microgravity. In *Twenty-Eighth Symposium (International) on Combustion*, pages 2843–2849. Combustion Institute, Pittsburgh, Pennsylvania, 2000. 4
- [13] K. Prasad, Y. Nakamura, S.L. Olson, O. Fujita, K. Nishizawa, K. Ito, and T. Kashiwagi. Effect of Wind Velocity on Flame Spread in Microgravity. In *Twenty-Ninth Symposium (International) on Combustion*, pages 2553–2560. Combustion Institute, Pittsburgh, Pennsylvania, 2002. 4
- [14] Y. Nakamura, T. Kashiwagi, K.B. McGrattan, and H.R. Baum. Enclosure Effects on Flame Spread over Solid Fuels in Microgravity. *Combustion and Flame*, 130:307–321, 2002. 4
- [15] W.E. Mell, K.B. McGrattan, and H.R. Baum. g-Jitter Effects on Spherical Diffusion Flames. *Microgravity Science and Technology*, 15(4):12–30, 2004. 4
- [16] A. Mukhopadhyay and I.K. Puri. An Assessment of Stretch Effects on Flame Tip Using the Thin Flame and Thick Formulations. *Combustion and Flame*, 133:499–502, 2003. 4
- [17] A. Hamins, M. Bundy, I.K. Puri, K.B. McGrattan, and W.C. Park. Suppression of Low Strain Rate Non-Premixed Flames by an Agent. In *Proceedings of the 6th International Microgravity Combustion Workshop, NASA/CP-2001-210826*, pages 101–104. National Aeronautics and Space Administration, Lewis Research Center, Cleveland, Ohio, May 2001. 4
- [18] K.B. McGrattan, R.G. Rehm, and H.R. Baum. Fire-Driven Flows in Enclosures. *Journal of Computational Physics*, 110(2):285–291, 1994. 4
- [19] P. Friday and F. W. Mowrer. Comparison of FDS Model Predictions with FM/SNL Fire Test Data. NIST GCR 01-810, National Institute of Standards and Technology, Gaithersburg, Maryland, April 2001. 6
- [20] A. Bounagui, N. Benichou, C. McCartney, and A. Kashef. Optimizing the Grid Size Used in CFD Simulations to Evaluate Fire Safety in Houses. In *3rd NRC Symposium on Computational Fluid Dynamics, High Performance Computing and Virtual Reality*, pages 1–8, Ottawa, Ontario, Canada, December 2003. National Research Council, Canada. 6
- [21] R.L. Alpert. *SFPE Handbook of Fire Protection Engineering*, chapter Ceiling Jet Flows. National Fire Protection Association, Quincy, Massachusetts, 3rd edition, 2003. 6
- [22] A. Bounagui, A. Kashef, and N. Benichou. Simulation of the Dynamics of the Fire for a Section of the L.H.-La Fontaine Tunnel. IRC-RR- 140, National Research Council Canada, Ottawa, Canada, K1A0R, September 2003. 6
- [23] Y. Xin. Assessment of Fire Dynamics Simulation for Engineering Applications: Grid and Domain Size Effects. In *Proceedings of the Fire Suppression and Detection Research Application Symposium, Orlando, Florida*. National Fire Protection Association, Quincy, Massachusetts, 2004. 6
- [24] J.A. Ierardi and J.R. Barnett. A Quantitative Method for Calibrating CFD Model Calculations. In *Proceedings of the CIB-CTBUH International Conference on Tall Buildings*, pages 507–514. International Council for Research and Innovation in Building and Construction (CIB), 2003. 6
- [25] G. Heskestad. *SFPE Handbook of Fire Protection Engineering*, chapter Fire Plumes, Flame Height and Air Entrainment. National Fire Protection Association, Quincy, Massachusetts, 3rd edition, 2002. 6



- [26] N.M. Petterson. Assessing the feasibility of reducing the grid resolution in fds field modeling. Fire Engineering Research Report 2002/6, University of Canterbury, Christchurch, New Zealand, March 2002. 6
- [27] A. Musser, K. B. McGrattan, and J. Palmer. Evaluation of a Fast, Simplified Computational Fluid Dynamics Model for Solving Room Airflow Problems. NISTIR 6760, National Institute of Standards and Technology, Gaithersburg, Maryland, June 2001. 6
- [28] National Institute of Standards and Technology, Gaithersburg, Maryland, USA, and VTT Technical Research Centre of Finland, Espoo, Finland. *Fire Dynamics Simulator, Technical Reference Guide*, 5th edition, October 2007. NIST Special Publication 1018-5 (Four volume set). 7
- [29] W. Zhang, A. Hamer, M. Klassen, D. Carpenter, and R. Roby. Turbulence Statistics in a Fire Room Model by Large Eddy Simulation. *Fire Safety Journal*, 37:721–752, 2002. 7
- [30] J. Smagorinsky. General Circulation Experiments with the Primitive Equations. I. The Basic Experiment. *Monthly Weather Review*, 91(3):99–164, March 1963. 7
- [31] J.W. Deardorff. Numerical Investigation of Neutral and Unstable Planetary Boundary Layers. *Journal of Atmospheric Sciences*, 29:91–115, 1972. 7
- [32] M. Germano, U. Piomelli, P. Moin, and W.H. Cabot. A Dynamic Subgrid-Scale Eddy Viscosity Model. *Physics of Fluids A*, 3(7):1760–1765, 1991. 7
- [33] D.K. Lilly. A Proposed Modification of the Germano Subgrid-Scale Closure Method. *Physics of Fluids A*, 4(3):633–635, 1992. 7
- [34] J. Hietaniemi, S. Hostikka, and J. Vaari. FDS Simulation of Fire Spread – Comparison of Model Results with Experimental Data. VTT Working Papers 4, VTT Building and Transport, Espoo, Finland, 2004. 8
- [35] C. Lautenberger, G. Rein, and C. Fernandez-Pello. The application of a genetic algorithm to estimate the material properties for fire modeling from bench-scale fire test data. *Fire Safety Journal*, 41:204–214, 2006. 8
- [36] J.C. Adams, W.S. Brainerd, J.T. Martin, B.T. Smith, and J.L. Wagener. *Fortran 95 Handbook: Complete ISO/ANSI Reference*. MIT Press, Cambridge, Massachusetts, 1997. 9
- [37] R. McDermott. A nontrivial analytical solution to the 2-d incompressible Navier-Stokes equations. [http://randy.mcdermott.googlepages.com/NS\\_exact\\_soln.pdf](http://randy.mcdermott.googlepages.com/NS_exact_soln.pdf), 2003. 11
- [38] G. Comte-Bellot and S. Corrsin. Simple Eulerian time correlation of full- and narrow-band velocity signals in grid-generated, ‘isotropic’ turbulence. *J. Fluid Mech.*, 48:273–337, 1971. 15
- [39] Stephen M. de Bruyn Kops. *Numerical simulation of non-premixed turbulent combustion*. PhD thesis, The University of Washington, 1999. 15
- [40] R. McDermott, A. Kerstein, R. Schmidt, and P. Smith. Characteristics of 1D spectra in finite-volume large-eddy simulations with ‘one-dimensional turbulence’ subgrid closure. In *American Physical Society, Division of Fluid Dynamics, Chicago, IL*, [http://randy.mcdermott.googlepages.com/implied\\_filter.pdf](http://randy.mcdermott.googlepages.com/implied_filter.pdf), Nov. 2005. 15, 16
- [41] Y. Morinishi, T. S. Lund, O. V. Vasilyev, and P. Moin. Fully conservative high order finite difference schemes for incompressible flow. *J. Comp. Phys.*, 143:90–124, 1998. 15

- [42] F. E. Ham, F. S. Lien, and A. B. Strong. A fully conservative second-order finite difference scheme for incompressible flow on non-uniform grids. *J. Comp. Phys.*, 177:117–133, 2002. 15
- [43] R. McDermott. Discrete kinetic energy conservation for variable-density flows on staggered grids. In *American Physical Society, Division of Fluid Dynamics, Salt Lake City, UT*, [http://randy.mcdermott.googlepages.com/aps2007\\_notes.pdf](http://randy.mcdermott.googlepages.com/aps2007_notes.pdf), Nov. 2007. 15
- [44] R. McDermott and S. B. Pope. A particle formulation for treating differential diffusion in filtered density function methods. *J. Comp. Phys.*, 226(1):947–993, 2007. 18
- [45] M. Germano, U. Piomelli, P. Moin, and W. Cabot. A dynamic subgrid-scale eddy viscosity model. *Phys. Fluids A*, 3(7):1760–1765, 1991. 18, 20
- [46] M. Pino Martin, U. Piomelli, and G. Candler. Subgrid-scale models for compressible large-eddy simulation. *Theoret. Comput. Fluid Dynamics*, 13:361–376, 2000. 18
- [47] P. Moin, K. Squires, W. Cabot, and S. Lee. A dynamic subgrid-scale model for compressible turbulence and scalar transport. *Phys. Fluids A*, 3(11):2746–2757, 1991. 18
- [48] T. S. Lund. On the use of discrete filters for large eddy simulation. Center for Turbulence Research Annual Research Briefs, 1997. 18
- [49] R. McDermott. Variable density formulation of the dynamic smagorinsky model. [http://randy.mcdermott.googlepages.com/dynsmag\\_comp.pdf](http://randy.mcdermott.googlepages.com/dynsmag_comp.pdf), 2004. 18
- [50] Stephen B. Pope. *Turbulent Flows*. Cambridge, 2000. 18, 20, 21
- [51] S.B. Pope. Ten questions concerning the large-eddy simulation of turbulent flows. *New Journal of Physics*, 6:1–24, 2004. 19
- [52] J. S. Baggett. Some modeling requirements for wall models in large eddy simulation. *Stanford Center for Turbulence Research Annual Research Briefs*, 1997. 20
- [53] J. S. Baggett. On the feasibility of merging LES with RANS for the near-wall region of attached turbulent flows. *Stanford Center for Turbulence Research Annual Research Briefs*, 1998. 20
- [54] W. Cabot. Large-eddy simulations with wall models. *Stanford Center for Turbulence Research Annual Research Briefs*, 1995. 20
- [55] Pierre Sagaut. *Large Eddy Simulation for Incompressible Flows*. Springer, 2001. 20, 21
- [56] H. Werner and H. Wengle. Large-eddy simulation of turbulent flow over and around a cube in a plate channel. In *8th Symposium on Turbulent Shear Flows*, pages 155–168, 1991. 20, 21
- [57] <http://www.fire.nist.gov/wui>. 20
- [58] L. F. Moody. Friction factors for pipe flow. *Transactions of the ASME*, 66, 1944. 20
- [59] K.B. McGrattan, S. Hostikka, J.E. Floyd, H.R. Baum, R.G. Rehm, W.E. Mell, and R. McDermott. Fire Dynamics Simulator (Version 5), Technical Reference Guide, Volume 1: Mathematical Model. NIST Special Publication 1018-5, National Institute of Standards and Technology, Gaithersburg, Maryland, October 2007. 20
- [60] H. Tennekes and J. L. Lumley. *A First Course in Turbulence*. MIT Press, 1972. 21

- [61] M. V. Zagarola and A. J. Smits. Scaling of the mean velocity profile for turbulent pipe flow. *Phys. Rev. Lett.*, 78:239–242, 1997. [21](#)
- [62] <http://code.google.com/p/fds-smv/source/browse/#svn/trunk/FDS/trunk>. [22](#), [23](#)
- [63] Bruce R. Munson, Donald F. Young, and Theodore H. Okiishi. *Fundamentals of Fluid Mechanics*. John Wiley and Sons, 1990. [23](#), [24](#)
- [64] R. Siegel and J. R. Howell. *Thermal Radiation Heat Transfer*. Taylor & Francis, New York, 4th edition, 2002. [27](#), [28](#)
- [65] Y.B. Zel’dovich and Y.P. Raizer. *Physics of shock waves and high-temperature hydrodynamic phenomena*. Dover Publications, New York, 2002. Translated from the Russian and then edited by W.D.Hayes and R.F. Probstein. [29](#), [30](#)
- [66] D. Drysdale. *An Introduction to Fire Dynamics*. John Wiley and Sons, New York, 2nd edition, 2002. [32](#)
- [67] H.S. Carslaw and J.C. Jaeger. *Conduction of Heat in Solids*. Oxford University Press, 2nd edition, 1959. [32](#)
- [68] K.W. Childs. HEATING 7: Multidimensional, Finite-Difference Heat Conduction Analysis Code System. Technical Report PSR-199, Oak Ridge National Laboratory, Oak Ridge, TN, 1998. [33](#)